Signiture, Supervisor

TECHNISCHE UNIVERSITÄT WIEN
Vienna University of Technology

DIPLOMARBEIT

Investigations on applying the time-of-flight method using cost effective hybrid Cherenkov radiators/scintillators for positron emission tomography

performed at the Institute for Atomic and Subatomic Physics
at the Vienna University of Technology

under supervision of
Univ.Prof. civ.ing. tekn.lic. tekn.dr. Lembit Sihver
Univ.Ass. Dipl.-Ing. Dr.techn. Albert Hirtl
Assistant Prof. Dennis R. Schaart, PhD
Dipl.-Ing. Dr.techn. Stefan E.K. Brunner

by

Michael Gruber, Matr.-Nr. 1028670, 066 461

Vorstadt 4, 3441 Abstetten, Austria

February 5, 2018

Signiture, Student

Acknowledgements

First of all i want to thank Prof. Lembit Sihver for his supervision of my work for this thesis.

I am also grateful for the supervision of Albert Hirtl and Stefan Brunner. It was inspiring to speak, write and work with you. The countless discussions have immensely influenced and improved this work. It was a pleasure to write this thesis with you as supervisor.

Last and foremost, I would like to thank my family, which made it possible for me to study at all, and my girlfriend Lara, who has tirelessly helped me with my thesis. Your support has brought me to where I am now.

Thank you!

Contents

1 Introduction

Positron annihilation detection is a method often used in the fields of physics and medicine. For a better resolution and sensitivity the detector systems have to be optimized. Particularly in medicine, where, for example, the method is used in time-of-flight positron emission tomography (TOF-PET), a higher resolution and sensitivity can significantly contribute to a quality improvement of diagnostics [1].

In recent years, the solid state silicon photomultiplier (SiPM) has been developed as an alternative to conventional photomultiplier tubes (PMT). Compared to PMTs, SiPM provide better timing properties and advantages, such as insensitivity towards magnetic fields. This results in new application possibilities such as the combined imaging methods like PET Magnetic Resonance Tomography (PET-MRT). A further development of the SiPM is the digital SiPM (dSiPM), which has the advantage of on-chip integration of the readout electronics which allows signal digitization at an early stage of the signal processing. In this thesis a dSiPM developed by Philips, i.e. the digital photon counter (DPC), is investigated [2]. This dSiPM allows to address individual single photon avalanche diodes (SPAD).

BGO was state-of-the-art in the field of scintillation material for positron emission tomography (PET) in the 1990s. However, materials with a better response-time (better TOF resolution) and a better light output were developed at the end of this decade, triggering the replacement of BGO to be used in PET [3]. In recent years, an increasing number of research groups were investigating the use of the Cherenkov radiation for TOF-PET. Due to the almost instantaneous response of this radiation, a good TOF resolution might be achieved. The complexity is, that the light output of the Cherenkov radiation is very low (for photon energies of 511 keV $\sim$ 10 photons within overall time will be emitted). In PET, BGO has essential advantages towards other materials, such as high stopping power for gamma radiation due to a high effective atomic number, potential low prized production, a high photoelectric fraction, no intrinsic background activity, high transparency down-to the UV-range and a relatively high light output for Cherenkov radiation due to a high refractive index.

Based on these attributes, BGO and BSO (which has similar properties as BGO) can be considered as promising scintillator materials allowing to perform fast timing with Cherenkov radiation.

This work is is based on a previously created simulation, which was developed in the course of a master thesis and is part of the PALADIN project [4], which aims to improve coincidence timing performance in the range of sub-100 ps FWHM timing resolution [5]. The contribution of this work was to implement BSO as scintillation material to the simulation framework, investigate the influence of the detector properties and scintillator material on the coincidence resolving time (CRT) and compare experimental results with simulation.

Different experimental setups are compared with simulations performed within the GEANT4 framework [6]. At the beginning, the plausibility of the physics applied in the simulation is examined and compared with theoretical predictions. Furthermore, the simulation is adapted and compared to an experimental setup built and investigated at TU Delft [7]. A system with two DPC-tiles and a point source, which randomly generates 511 keV back-to-back photons is created. According to the experimental setup, scintillator crystals with a base area of 3 x 3 mm^2 and variable

lengths were simulated.

The data obtained from the simulation are analyzed with a self developed tool, created within the framework ROOT [8].

2 Background

In this chapter the technical background, physical background and underlying mathematical models are outlined. At the beginning, the Monte Carlo method and the frameworks GEANT4 and ROOT are described. Further on, the different processes of interaction of photons in matter and their effects are briefly discussed in the energy range eV to few 100 keV. The following chapter briefly explains the interaction of photons at interfaces. Additionally different models which are provided by GEANT4 to simulate interactions at optical interfaces are described in more detail. At the end of this chapter, the underlying processes of scintillation and Cherenkov radiation and the main characteristics of dSiPMs are explained in detail.

2.1 Monte Carlo method

Monte Carlo techniques are stochastic computational procedures, which approximate a solution iteratively via the repeated generation of random numbers. The Monte Carlo method is usually used in optimization, numerical integration and in generating draws from a probability distribution (e.g., problems with a high number of degrees of freedom). Thereby, solutions to analytically insolvable or with the present technology not yet computable problems can be approximated with this method. These solutions can vary with a certain probability compared to the numerical exact solution. The error compared to the exact solution is decreasing with a higher number of calculation steps. A fundamental component of the Monte Carlo method is the generation of uniformly distributed random values $r_i \in [0;1)$, which, in a next step, are used to generate random values following any specific distribution (probability density function - PDF) [9].

Let N_0 be a uniformly distributed PDF which generates a sequence of random numbers r_i, with $0 < r_i < 1, i \in \mathbb{N}_0$. These numbers are used to create a series x_i, which is distributed according to the PDF $f(x)$. F and G are the cumulative distributions of the corresponding PDFs f and g, respectively . The conventionally used method is the transformation method. Here, a function $x(r)$, distributed according to the function $f(x)$, with $0 < r_i < 1 \sim N_0$ is unknown. The probability of obtaining a number r, in the interval $[r, r+dr]$ is equivalent to $g(r)dr$. Furthermore, the probability of generating a value x in the corresponding Interval $[x(r), x(r)+dx(r)]$ is the same.

$$F(x(r)) = \int_{-\infty}^{x(r)} f(x')dx' = \int_{-\infty}^{r} g(r')dr' = r \tag{1}$$

With the inversion problem:

$$x(r) = F^{-1}(r) \tag{2}$$

The PDFs usually have finite limit values, e.g. $f(x)$ is defined in the interval $[a, b]$ and $g(r)$ in the interval $[c, d]$. This means:

$$f(x) \begin{cases} \neq 0, \ a \leq x \leq b \\ = 0, \ \text{otherwise} \end{cases} \quad \wedge \ g(r) \begin{cases} \neq 0, \ c \leq r \leq d \\ = 0, \ \text{otherwise} \end{cases}$$

$$\int_a^b f(x')dx' = \int_c^d g(r')dr' = 1$$

In most cases it is either not possible, or difficult to solve Equation (2) analytically. A useful alternative is the rejection method. This method can generate a set of values $\vec{x}$ distributed according to the PDF $f(x)$ by multiple iterations. The sequence is:

1. generation of a random number x uniformly distributed between $x_{\min}$ and $x_{\max}$ with a uniformly distributed random number $r_1 \in [0, 1]$ by: $x = x_{\min} + r_1(x_{\max} - x_{\min})$
2. generation of a random number u uniformly distributed between 0 and $f_{\max}$, with $u = r_2 f_{\max}$
3. accept x if $u < f(x)$, otherwise reject and repeat

A higher acceptance can be achieved by approximating the PDF $g(x)$ to $f(x)$ since the probability depends on the ratio of the surfaces of both curves. In Figure (1a) and (1b) 1000 Points $P_i(x_i, y_i)$ are generated. The x-coordinates are randomly distributed over the range of $(-2, 2)$ and the y-coordinates are distributed according to the PDF $g(x)$ with the respective x. Only points where $P_i(x_i, y_i) < f(x_i)$ are accepted (red dots). In further consequence the x-coordinates of these accepted points are distributed according to the PDF $f(x)$. The probability for the number of accepted points is increasing if the PDF $g(x)$ converges to the PDF $f(x)$ as shown in Figure 1.

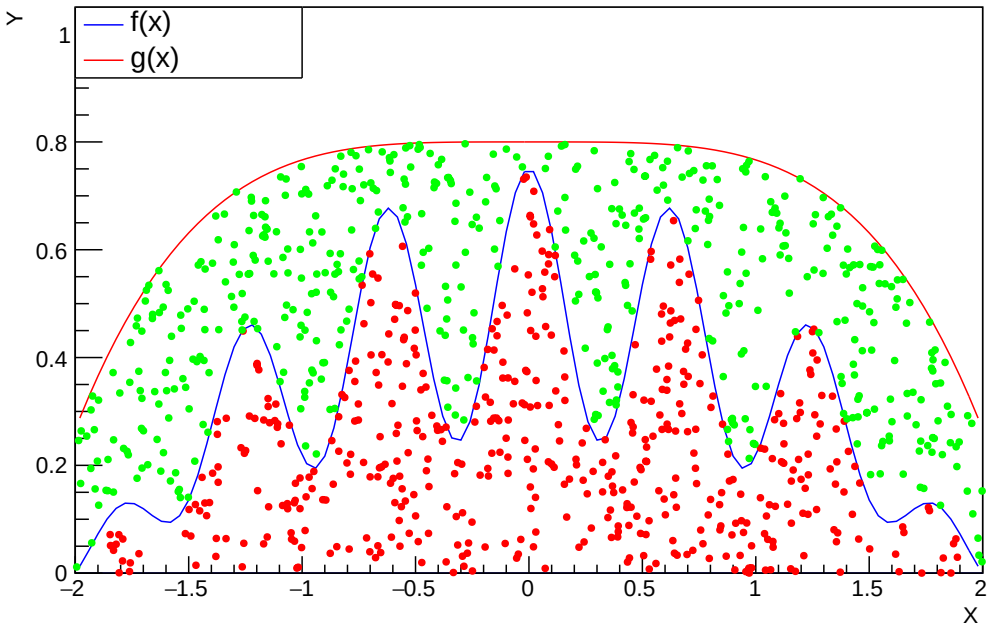

(a)

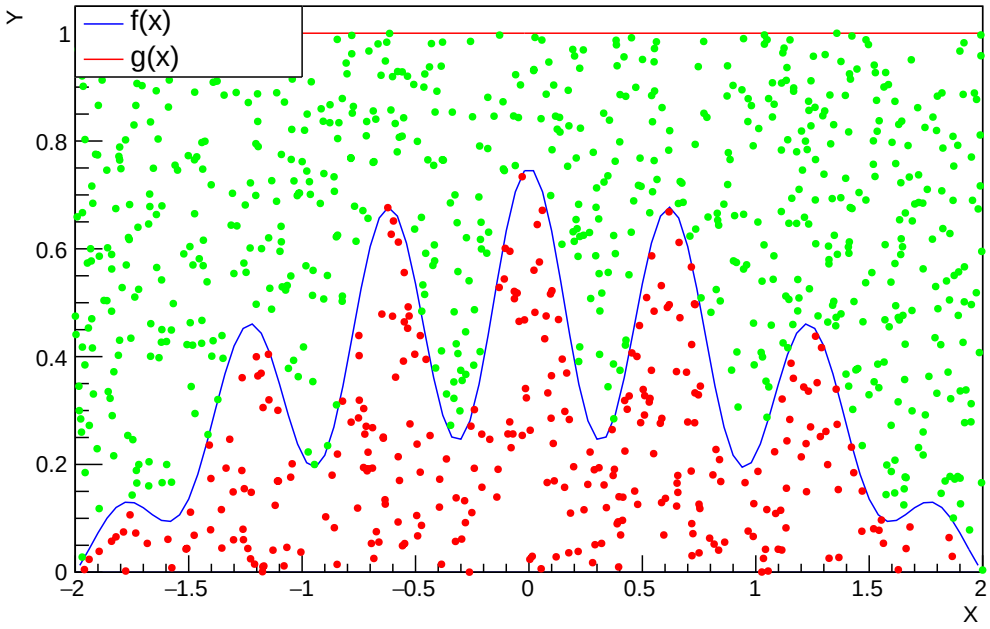

(b)

Figure 1: In both pictures 1000 points are generated, red dots are accepted and green dots are rejected points. In Figure (1a) the y-values of the respective dots are distributed according to the PDF $g(x)$ where 485 points are accepted. A uniformly distributed PDF $g(x)$ where 309 dots are accepted is shown in Figure (1b). In further consequence the accepted numbers x_i from the individual accepted points $P_i(x_i, y_i)$ are used as random numbers, distributed according to the PDF $f(x)$.

2.2 GEANT4 - a simulation framework

GEANT4 [6] is an object oriented C++ open source framework for the simulation of hadronic, electromagnetic and optical processes in matter in the energy range of a few eV to TeV and can calculate the transport and decay of many short- to long-lived particles and their interactions with most available targets. The application area is in high energy, nuclear and accelerator physics, as well as medical and space science.
GEANT4 contains a variety of physics models which are improved continuously, to create a correct simulation of the proceeding physical process in a wide energy range. By object-oriented programming it was possible to organize complex structures of the physical models in a consistent form.
GEANT4 ist structured into several categories: geometry and materials, particle interaction in matter, tracking management, digitisation and hit management, event and track management, visualisation and visualisation framework as well as user interface. For a flexible programming it is possible to use the classes provided by GEANT4 in a modular way. Three mandatory classes have to be defined for an executable simulation and are listed below [6]. In this work the "RanecuEngine" provided by GEANT4 is used for the generation of uniform distributed values.

Physics List

The class Physics List is responsible for defining the properties of all particles, the physical processes as well as the cut-off parameter, which has to be defined to avoid infrared divergence. Due to the massive complexity of the physical processes of all particles and their interaction with matter in the energy range of eV to TeV, there are no generally valid algorithms for every problem. Therefore the user has to select a Physics List, which provides the optimal solution for a certain problem. It is also possible to use a custom physics list, which is adapted to the problem.

Primary Generator

In this class the primary vertices are defined and the primary particles are generated. The user has to define a specific vertex per event, which is the source of the examined particles. The direction, the energy and the number of particles must be specified. Additionally, it is possible to simulate a radioactive source with a certain volume.

Detector Construction

The geometry of the detector, materials, detector sensitivities and visual attributes are defined here. In this process, geometric shapes are created first, then certain materials are assigned to them. There are predefined material tables where each individual composition of elements can be created. After assigning a material and its properties to a geometry is must be positioned in the simulation geometry, called world. Volumes can be defined as sensitive detectors which are used for data acquisition.

The procedural structure in GEANT4 can be subdivided into four processes [10, 5]:

Run

The run is the largest unit of the simulation and is managed by the G4RunManager singleton class which handles: the initialization of the application, number of events and starts/aborts a run. Changes in fundamental definitions like geometry of the detector and physics list have

to be done prior to the initialization of the application. During a run the geometry of the detector, the physics list and the setup of sensitive detector should be fixed.

Event

The event is an object of the class G4EventManager and is constructed by G4RunManager. It has four main information types:

- primary vertex and primary particle
- trajectories
- hits Collections
- digits Collections

The event manages all processes of a primary particle and its secondary particles. If all tracks are gone, e.g. by absorption or get killed by reaching the boundary of the world the of simulation, the event ends. This object exists only inside the class G4RunManager.

Track

The track contains current information like position and energy of the particle during an event. Only processes, e.g. Compton scattering or photoelectric effect, can change information about the track or generate secondary tracks. Each particle has its own unique track with track ID. Thereby the trajectory or other information of a unique particle through the world can be stored and reconstructed. Tracks exists only inside the event they were created in. Data about the track are stored in the class G4Track.

Step

The step is the smallest unit of the simulation. The track of a particle consists of a sequence of steps. Furthermore a step is defined by two points, the PreStepPoint and the PostStepPoint, which contain the coordinates in the world and the volume containing these points. The step length depends on geometrical and physical properties. If a particle is going to transit through two different materials, the PostStepPoint gets set at the boundary of this two volumes and the next step continues from there. Furthermore the step length gets adapted by a Monte Carlo method which considers the probability of interaction of the particle with matter.

2.3 ROOT - an analysis framework

ROOT [8] is an open-source software, programmed in C++ and custom built for efficiently storing, accessing and manipulating extremely large data sets. Multidimensional histograms, fits, 3D visualization, 2D-3D plots, et.c. can be created. Furthermore many statistical tools for data analysis are available. Additionally, ROOT provides a graphical interface which can be used to handle data directly without the development of a C++ script.
The structure of ROOT uses the concept of trees which are based on the anatomy of a tree. Thus, more complex raw data can be analyzed. A tree is made of Branches and a Branch has several Leafs which can be variables, structures, arrays or objects. It is possible that a ROOT, file contains several trees (e.g. data sets of several measurements of an experimental set-up), every tree contains several branches (subdivision of a measurement) and every branch contains several leaves (simple

data files with entries in rows and columns) [8].

2.4 Physical background

In this chapter, the essential physical processes are explained.

2.4.1 Interaction of photons in matter

The type and probability of interaction between photons and matter depends on various factors, such as density, atomic number and energy of the incoming photon. There is always a dominant interaction which depends on the energy of the photon and the atomic number of the element. In Figure 2, different possibilities for the interaction of photons in matter with the respective cross section, as a function of the energy for BGO, are plotted. Figure 3 shows the dominant interaction as a function of the energy of the photon and the atomic number of the matter in which the interaction takes place. Furthermore, only the interactions occurring in the energy range between a few eV to few 100 keV are discussed in more detail below, which is the energy range of electron-positron annihilation, scintillation and Cherenkov photons. Coherent scattering and nuclear pair-production will not be explained in more detail, as they have no relevant influence on this work.

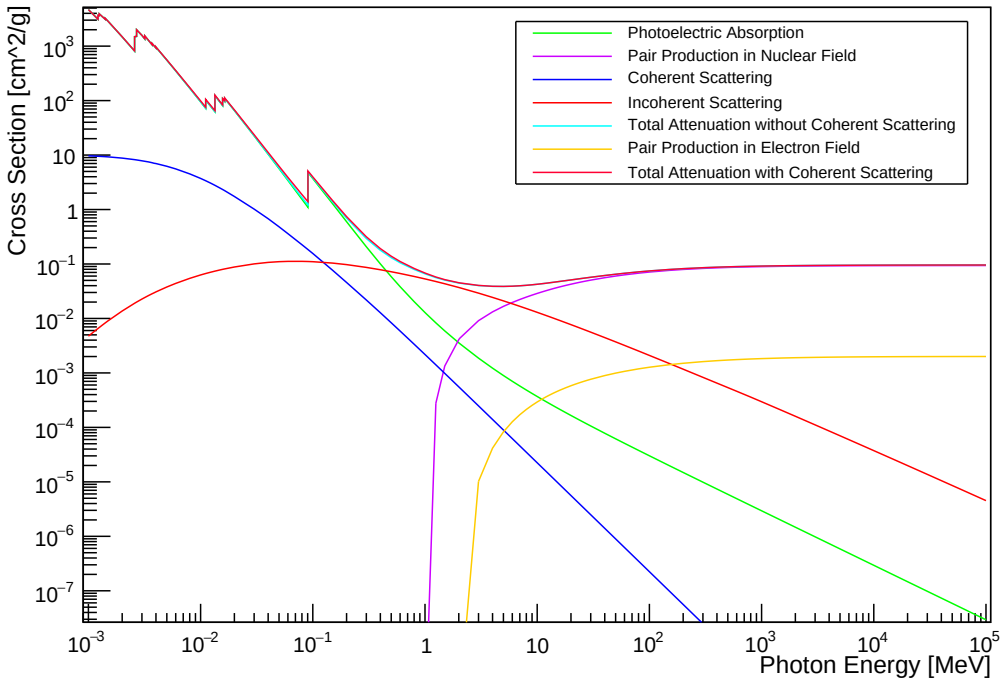

Figure 2: Different forms of interaction between photons and matter and their cross sections as a function of energy. The used data sets are calculated from XCOM [11] for $Bi_4Ge_3O_{12}$, (BGO).

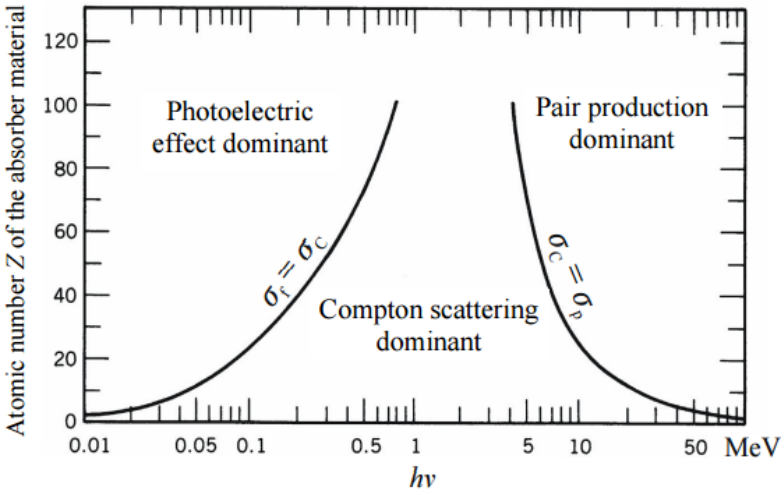

Figure 3: Illustration of the dominant interaction mechanism in dependence of the atomic number of the material and photon energy [12].

2.4.1.1 Photoelectric effect

The photoelectric effect is dominant in the lower energy range. The probability of the interaction can be approximated according to [13]

$$\sigma_f \cong \text{const} \cdot \frac{Z^n}{E_\gamma^{3.5}}, \tag{3}$$

while σ_f is the probability for photoelectric absorption, Z is the atomic number, n is a constant varying between four and five and E_γ is the photon energy. As illustrated in Figure 4, an electron from a deep electron shell is lifted from a bound state to an unbound state and thereby completely absorbs the incoming photon. The electron now has the kinetic energy $E_{\text{kin}} = E_\gamma - E_{\text{bound}}$, where E_{bound} is the binding energy of the electron in the atom.

The characteristic spikes of the cross section according to an element shown in Figure 2, are caused by the discrete binding energies of the different electron shells.

2.4.1.2 Compton scattering

At higher photon energies the dominant effect is the Compton scattering. In this interaction a photon is inelastically scattered at an outer shell electron. Thereby, the electron is lifted from a bound state to a free state, as shown in Figure 5. The scattered photon has an energy, depending on the scattering angle θ. The dependence of the photon energy on the scattering angle can be written as

$$E'_\gamma = \frac{E_\gamma}{1 + \frac{E_\gamma}{m_0 c^2}(1 - cos(\theta))}, \tag{4}$$

while E'_γ is the scattered photon energy, E_γ is the incoming photon energy, $m_0 c^2$ is the rest energy of an electron and θ is the scattering angle. The probability for Compton scattering is linearly proportional to the atomic number.

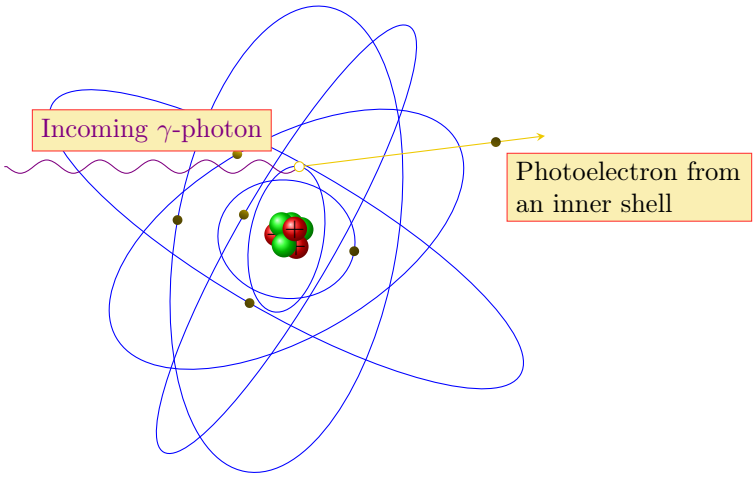

Figure 4: Illustration of the photo electric effect [14]. An electron from a deep electron shell gets excited form a bound state to an unbound state by absorption of an incoming photon.

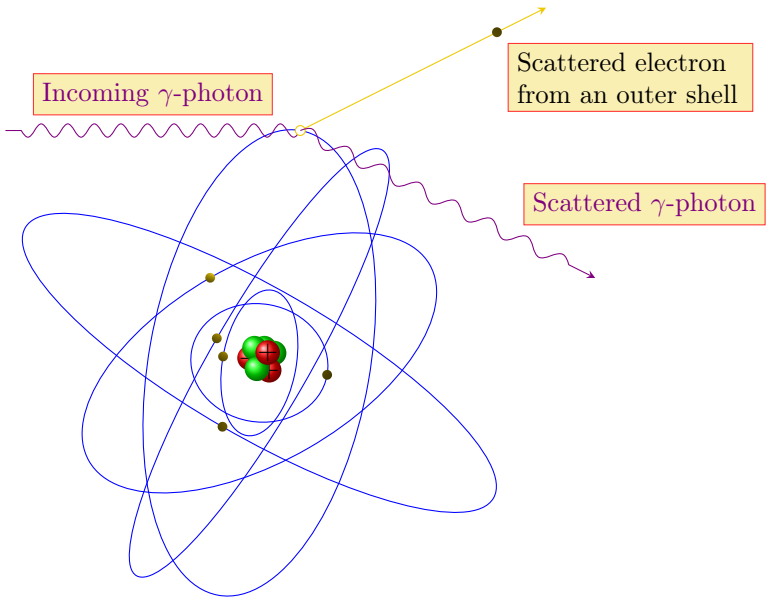

Figure 5: Illustration of Compton scattering [14]. An electron from an outer shell gets excited from a bound state to an unbound state by inelastic scattering of an incoming photon. The photon energy after scattering is dependent on the scattering angle θ.

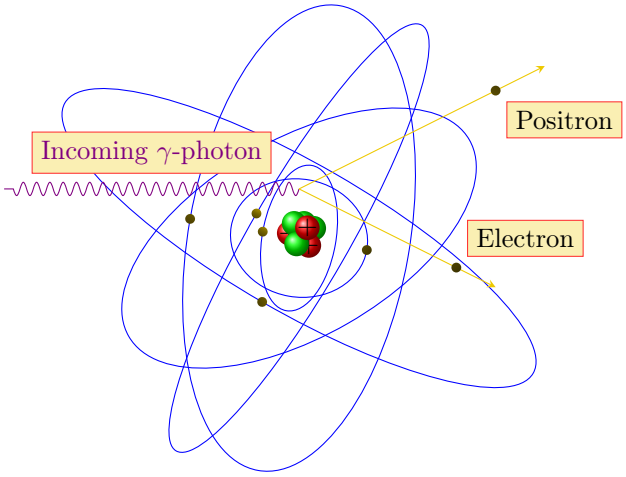

Figure 6: Illustration of the electron pair production [14]. A photon with an energy greater than two times the rest energy of an electron creates an electron-positron pair within the electro-magnetic field of the atomic nucleus.

2.4.1.3 Electron pair production

In pair-production, the photon interacts with the Coulomb-field of the atomic nucleus. Thereby, the photon is transformed into an electron-positron pair as shown in Figure 6. This effect can only proceed if the kinetic energy of the photon is greater than two times the rest energy of an electron (511 keV) and is the dominant interaction for high energy photons with energies of a few MeV and more. The probability of this interaction is proportional to Z^2. After the creation of the pair, electron and positron have the kinetic energy $E_{\text{kin}} = E_\gamma - 1022\,\text{keV}$.

2.4.2 Photons at boundary surfaces between two media

This subsection briefly explains the properties of photons at interfaces between two media. Furthermore, the models for the calculation of these effects, used in GEANT4, are discussed and their differences are explained.

The processes proceeding at an interface are absorption, reflection and transmission which are dependent on the media and the direction of the photon. The interface can basically be distinguished in two cases: dielectric-dielectric and dielectric-metal. In general, a medium i has a complex refractive index $n_i = n_{ir} - i\kappa_i$, whereas the imaginary part for transparent media is negligibly small (low absorption) which is also done in the case of two media with low absorption.

Dielectric-Dielectric

In this case, a photon is located in a medium 1 with the refractive index $n_1 = n_{1r}$, and enters the interface to a medium 2 with $n_2 = n_{2r}$ under an incident angle θ_i. When reaching the interface reflection and transmission can occur. When the photon is reflected it has a reflection angle θ_r, which is identical to the angle of incidence θ_i ($\theta_r = \theta_i$). When it is transmitted, the photon moves further in the medium 2 but is rotated with an angle θ_t from the primary path (refraction). An incoming photon which is reflected or refracted is shown

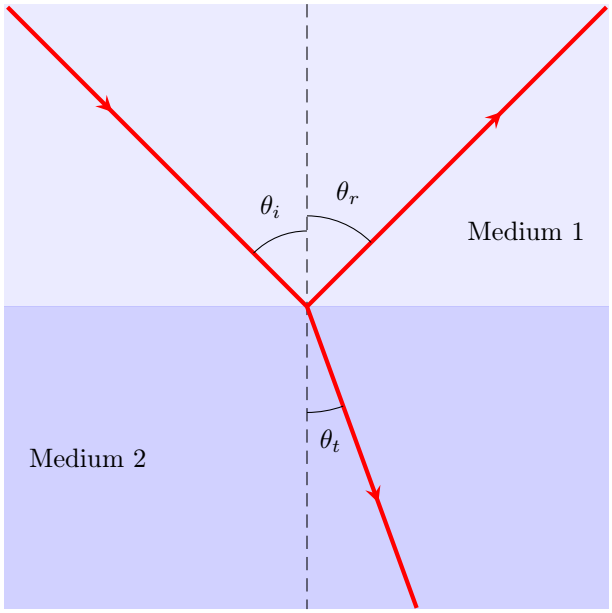

Figure 7: An incident photon gets reflected or refracted at the boundary layer.

in Figure 7. The correlation between the angle of refraction and the refraction index of the two-dimensional medium is given by [15]

$$\frac{sin(\theta_i)}{sin(\theta_t)} = \frac{n_2}{n_1}. \tag{5}$$

For an incident photon interacting with a boundary layer between two dielectric materials with refraction indices n_1 and n_2, the reflection and transmission coefficients are calculated using the Fresnel-equation. The vertically polarized component R_s/T_s is calculated with Equation (6) and the parallel component is calculated with Equation (7)

$$R_s = \left(\frac{n_1 cos(\theta_i) - n_2 cos(\theta_t)}{n_1 cos(\theta_i) + n_2 cos(\theta_t)}\right)^2 \qquad T_s = \frac{n_2 cos(\theta_t)}{n_1 cos(\theta_i)} \left(\frac{2 n_1 cos(\theta_i)}{n_1 cos(\theta_i) + n_2 cos(\theta_t)}\right), \tag{6}$$

$$R_p = \left(\frac{n_2 cos(\theta_i) - n_1 cos(\theta_t)}{n_2 cos(\theta_i) + n_1 cos(\theta_t)}\right)^2 \qquad T_p = \frac{n_2 cos(\theta_t)}{n_1 cos(\theta_i)} \left(\frac{2 n_1 cos(\theta_i)}{n_2 cos(\theta_i) + n_1 cos(\theta_t)}\right). \tag{7}$$

Dielectric-Metal

The imaginary part of the refraction index (κ) for metals is generally larger compared to the real part of the index (n') and not negligible, as for dielectrics (n_2). The reflectivity can be simplified to

$$R = \left|\frac{n' - i\kappa - n_2}{n' - i\kappa + n_2}\right|^2 \tag{8}$$

for vertical incidence of photons on a boundary layer. However, metals with a high reflectivity correspond with a large complex refraction index (high absorption).

GEANT4 uses different models to calculate the boundary layer properties between two different

media, which are discussed in more detail in the next sections.

2.4.2.1 Glisur model

The Glisur model is the simplest form to simulate an interface between two materials. The reflectivity and the surface finishes *polished* or *ground* serve as parameter, as well as its roughness parameter *polish*, which can attain values between 0 and 1. At surface type *polished*, a perfectly smooth interface is simulated whereas at type *ground* a random vector in a circle with radius $1 - polish$ is generated (1 means perfectly polished surface) which is added to the average normal vector of the reflected photon. For each reflection that proceeds such a surface-normal is generated. The incident photon is reflected at the interface specularly. The reflection coefficient can take values between 0 and 1 for different energies. As the refractive indices are disregarded in this model, it is mainly used for the simulation of dielectric-metal boundary layers. When a photon is absorbed at the dielectric layer in GEANT4, the particle gets immediately eliminated, although it owns a certain penetration depth depending on the free path (very small for metals) [16].

2.4.2.2 Unified model

The Unified Model was developed for the program DETECT and in further progression for GEANT4 [17]. It is used for the correct simulation of optical photons at boundary layers between two materials. DETECT is a Monte Carlo based program, which was used for the simulation of scintillation detectors. The Unified model owns seven variable parameters, explained below in more detail, which can be adapted to the respective boundary layer. This may often seem to be difficult because the parameters are mostly unknown, and often complex experiments are necessary to adjust them for the simulation [17].

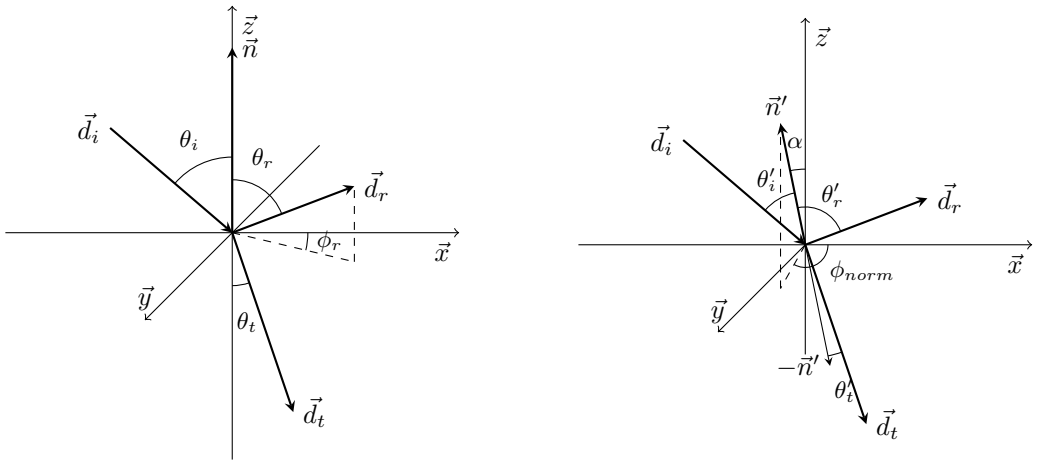

Figure 8: Coordinate systems with the geometrical parameter used in the Unified model. Figure (a) shows the coordinate system according to the average surface and Figure (b) shows the coordinate system according to the generated micro facet.

In this model the Fresnel equations are used to calculate the reflection coefficient as shown in

Equation (9), which depend on the refractive indices of the two media

$$R = \frac{1}{2}\left(\frac{sin^2(\theta_i' - \theta_t')}{sin^2(\theta_i' + \theta_t')} + \frac{tan^2(\theta_i' - \theta_t')}{tan^2(\theta_i' + \theta_t')}\right). \tag{9}$$

The transmission coefficient therefor is given by $T = 1 - R$.

It should by noticed that the angles θ_i' and θ_t' are relative to the surface normal of the micro-facet $\vec{n}'$ in Equation (9). For a better illustration, the used vectors and angles are shown in Figure 8. The vectors $\vec{d_i}$, $\vec{d_r}$ and $\vec{d_t}$ are the direction vectors of the incident, reflected and refracted photon. If the incident photon is reflected internally, the reflective angle is equal to the incident angle. In the case of refraction the photon gets refracted with a refraction angle following Snellius' law, as shown in Equation (5). At surface type *ground*, the reflection angle θ_r and the refraction angle θ_t follow a Lambertian distribution, which depends on the angle α, which is located between the micro-facet normal $\vec{n}'$ and average surface normal $\vec{n}$. There are four different options how a photon can be reflected at a boundary surface in the Unified model. In the case of specular spike reflection, the photon is reflected at the average surface normal, for specular lobe reflection the photon is reflected at the micro-facet normal, for Lambertian reflection the photon is reflected diffuse and for backscatter reflection the photon is reflected backward to the same direction from where the photon came, which occurs when the incident photon hits the micro-facet at a normal angle. In Figure 9, the different reflection probabilities are shown. By setting the probabilities for the corresponding reflection (the sum must be 1) the user is able to adjust the radiant intensity of the reflected photons which is calculated as follows

$$\begin{aligned} J(\theta_i, \theta_r, \phi_r) = \frac{d\phi}{d\omega} \approx R(\theta_r', n_1, n_2) * [C_{sl} g(\alpha_r; 0, \sigma_\alpha) + \\ C_{ss}\delta(\theta_i - \theta_r) + C_{bs}\delta(\theta_i + \theta_r) + C_{dl} cos(\theta_r)] + T(\theta_t', n_1, n_2) g(\alpha_t; 0, \sigma_\alpha). \end{aligned} \tag{10}$$

$J(\theta_i, \theta_r, \phi_r)$	radiant intensity of the reflected photons
ϕ_r	azimuth angle between the projection of the incident angle and the average surface
$d\phi/d\omega$	photon flux $d\phi$ passing through the solid angle $d\omega$
$g(\alpha_r; 0, \sigma_\alpha)$	gaussian distribution with standard deviation σ_α and mean 0 generating α_r
C_{sl}	specular lobe parameter, defines the probability of specular reflection at the micro-facet
C_{ss}	specular spike parameter, defines the probability of specular reflection at the average surface
C_{bs}	back scattering parameter, defines the probability of backward reflection at a micro-facet
C_{dl}	defuse lobe parameter, defines the probability of lambertian reflection
$T(\theta_t', n_1, n_2)$	transmission parameter, defines the probability of transmission
$g(\alpha_t; 0, \sigma_\alpha)$	gaussian distribution with standard deviation σ_α and mean 0 generating α_t

In the Unified model the micro-facets are defined by the angle α and ϕ_{norm}. The angle α is located between the average surface normal and micro-facet normal and is randomly generated

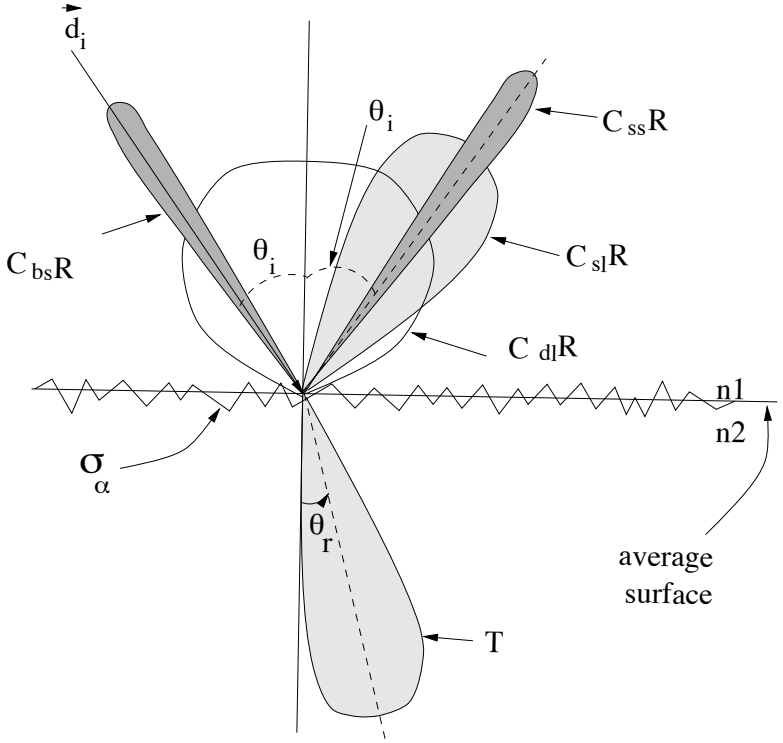

Figure 9: The reflection and transmission probabilities and angles of an incident photon between two materials are shown [17].

from a Gaussian distribution with standard deviation σ_α and mean 0. The angle ϕ_{norm} is the azimuth angle of the micro-facet normal and is represented in the XY-plane between the micro-facet projection and the x-axis, as shown in Figure 8b, which is generated by a uniform distribution between 0 and 2π. There are three special cases where new angles α and ϕ_{norm} must be created and thereby a new normal vector of the local micro-facet must be generated.

1. the scalar product between the incident photon vector and micro-facet normal is less than zero,

2. the scalar product between the refracted photon vector and the average surface normal is greater than zero,

3. the scalar product between the reflected photon vector and the average surface normal is less than zero.

2.4.2.3 Look-Up-Table model

As discussed in section 2.4.2.2, the free parameters are often unknown in the Unified model and have to be determined with considerable effort. In the field of scintillation detectors, several reflector materials are commonly used and therefore Look-Up-Tables (LUT) were created. The data used in the LUT are collected from measurements with BGO as a scintillation crystal [18]. Based on this data sets, the user does not need to remeasure the precise roughness parameter of

the surface to perform an accurate simulation. However, due to various errors, the LUT is not recommended for special simulations [19]. It can be selected from three different surface finishes, mechanically polished, chemically etched and rough-cut. Further, it can be choosen between six attached reflectors, non, Lumirror, Teflon, ESR film, Tyvek, or TiO_2 paint, as well as two bonding types, air-coupled or glued [10].

2.4.3 Scintillation

Scintillation is a luminescence process which has been used for a long time to detect ionizing radiation in a broad energy spectrum. There are different mechanisms which lead to luminescence, whereby in this thesis only those of inorganic scintillators are discussed in more detail. There are some characteristics an ideal scintillator should provide:

- high scintillation efficiency by converting the kinetic energy of a charged particle into detectable optical light,
- the emitted light yield should be linearly proportional to the deposited energy of the ionizing radiation in a wide range of energy,
- the scintillator should be transparent to its own emitted light,
- for fast timing applications, the decay time should be as short as possible,
- for the case of commercial products, cheap and easy production,
- the refractive index should be near that of glass for good optical coupling from the scintillator to a PMT or light sensor.

Depending on the application, a scintillator is used for, compromises must be made between these criteria. In general three types of scintillator material are distinguished: organic, inorganic and gaseous scintillators. Organic scintillators generally have a shorter decay time but a low density and are often used for beta spectroscopy and fast neutron detection because of their hydrogen content. Inorganic scintillators often have a better linearity and are preferred for gamma-ray detection because of their high atomic number and high density. Gaseous scintillators have a fast response time and consists of noble gases like helium, argon, krypton or xenon often with addition of nitrogen and are used to detect heavy charged particles. In further consequence, this type of detector will not be discussed in more detail.

In inorganic scintillators, electron-energies are within discrete energy bands. Energy bands in dielectric media are usually be populated up to the valence band. However, they can be excited to a higher state, the conduction band, after interaction, e.g. with a photon. Between these two bands there is a band gap where electron-energies are not allowed in pure crystals. Pure crystals are self-absorbing in the energy range of the band gaps when the electron is de-excited back into the valence band and is therefore not transparent. In addition, the energy of the generated photons is too high for most crystals and is therefore not in the sensitive energy range of the detector. There are two different scintillation mechanisms to produce optical photons which are not absorbed by the crystal itself: activated and self-activated scintillators. In both cases there are discrete energy levels in the band gap in which the excited state of the electron-hole pair can be located. The

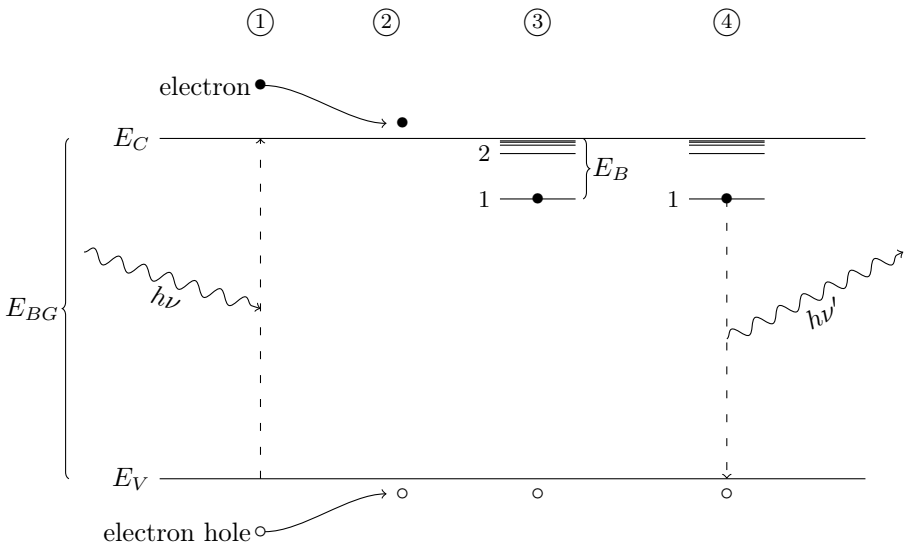

Figure 10: Schematic sketch of the scintillation process of a self-activated inorganic scintillator.
① creation of an electron-hole pair by an incident photon with energy $h\nu > E_{\mathrm{BG}}$
② free electron is cooled down by inelastic interactions, hole drifts to the top of the valence band
③ electron and hole build an exciton with binding energy E_{B}
④ electron and hole recombine and emit a photon with energy $h\nu' = E_{\mathrm{BG}} - E_{\mathrm{B}}$

electron-hole pair recombines, produces an optical photon with lower energy than the band gap of the crystal and thus has a sufficient free path length to be detected.

In activated inorganic scintillators, small amounts of impurities, called activator atoms, are added to the crystal lattice. Thereby, energy states within the forbidden energy gap are created. Along the transition path of ionizing radiation through a scintillator crystal, electron-hole pairs are generated. Holes will drift to activator sites and ionize them and electrons with high energy are cooled down to the bottom of the conduction band by inelastic interaction. Thereby, they could migrate quasi-freely through the crystal until they recombine with an ionized activator atom to an excited state and neutralize it. If the transition from the excited to the ground state of the activator atom is allowed, the electron will de-excite quickly and emit a corresponding photon. For a forbidden transition, the electron has to raise to a higher excited state from which the electron is allowed to de-excite by an increment of energy. Usually the thermal energy of the crystal is sufficient [1].

In self-activated inorganic scintillators, the holes drift to the top of the valence band while the electrons are cooled down to the bottom of the conduction band after several inelastic interactions and associate with each other to an exciton. An exciton is a quasiparticle that exists in insulators and semiconductors which can transport energy without transporting electrical charge, and is very similar to a hydrogen atom with lower binding energy because of the small effective mass. The exciton has discrete binding energy states and the decay depends on the overlap of the wave-functions of the electron and electron-hole. If the electron recombines with the electron-hole, a photon is emitted with the energy of the band gap, decreased by the binding energy of the exciton. The schematic process of the generation of optical photons by self-activated inorganic scintillator is illustrated in Figure 10.

2.4.4 Cherenkov radiation

The emission of photons created by a charged particle, passing through a dielectric material which has a velocity greater than the speed of light in that material is called Cherenkov effect. c_{m} is the speed of light in that material with $c_{\mathrm{m}} = \frac{c}{n(\omega)}$ where c is the speed of light in vacuum and $n(\omega)$ is the refractive index of the dispersive material. The required velocity for photon emission, v_{particle}, depends on the refractive index of the medium. Cherenkov radiation has a short response time compared to scintillator and is in the order of picoseconds. Therefor, the detector has to be exceptionally fast in order to make use of the fast response. Compared to scintillation emission, the Cherenkov radiation has a low average number of created photons. The average number of photons produced by a charged particle per track length with $v_{\mathrm{particle}} > c_{\mathrm{m}}$, ist calculated by

$$\frac{dN}{dx} = 2\pi z^2 \alpha \sin^2(\theta) \int_{\lambda 1}^{\lambda 2} \frac{d\lambda}{\lambda^2}. \tag{11}$$

The emission of electromagnetic waves, i.e. the Cherenkov photons, is created by polarization and consecutive depolarization of the surrounding atoms in the crystal lattice by a relativistic charged particle. If $v_{\mathrm{particle}} > c_{\mathrm{m}}$ the electromagnetic waves emitted by depolarization of the atoms can interfere constructively and therefor, photons can be emitted. A cone shaped wave front with a characteristic opening angle θ, called Cherenkov angle, as shown in Figure 11, is created, which is given by

$$cos(\theta) = \frac{1}{\beta n(\omega)}, \tag{12}$$

with $\beta = \frac{v_{\mathrm{particle}}}{c}$. The Cherenkov angle depends on the particle velocity and the refractive index, as shown in Equation (12).

2.5 Silicon photomultipliers

Silicon photomultipliers (SiPM) are silicon-based single photon avalanche diodes (SPAD) combined in an array. Compared to photomultiplier tubes (PMT), which have been developed since the 1940s and have almost exploited the technically feasible potential, SiPMs are at an earlier stage of technical development. SiPM have a higher detection efficiency, a higher gain, can be built compactly and are insensitive towards magnetic fields. Furthermore, they can be operated in a low voltage range, whereas PMTs for electron acceleration are operating in the range of kV and therefore need to be powered with higher safety-related attention [20]. A disadvantage and main reason for noise of SiPMs are thermically caused avalanches.

SPADs are p-n transition operated at a bias above the breakdown voltage. At this voltage charge carriers can be accelerated to a sufficient energy to generate additional electron-hole pairs. This effect proceeds cascading and results in a charge avalanche. The process of self-sustaining generation of electron-hole pairs can be suppressed (quenched) when decreasing the bias voltage with a quenching resistor R_q below the breakdown voltage [21].

A thermal electron can be generated and forms an avalanche due to the bias. The dark count rate (DCR) is defined as the time frequency of the thermic caused avalanches. Furthermore, a SiPM has a temperature-dependent gain and should therefore be operated at a constant temperature. Another factor which is responsible for a higher noise is the optical crosstalk between two SPADs,

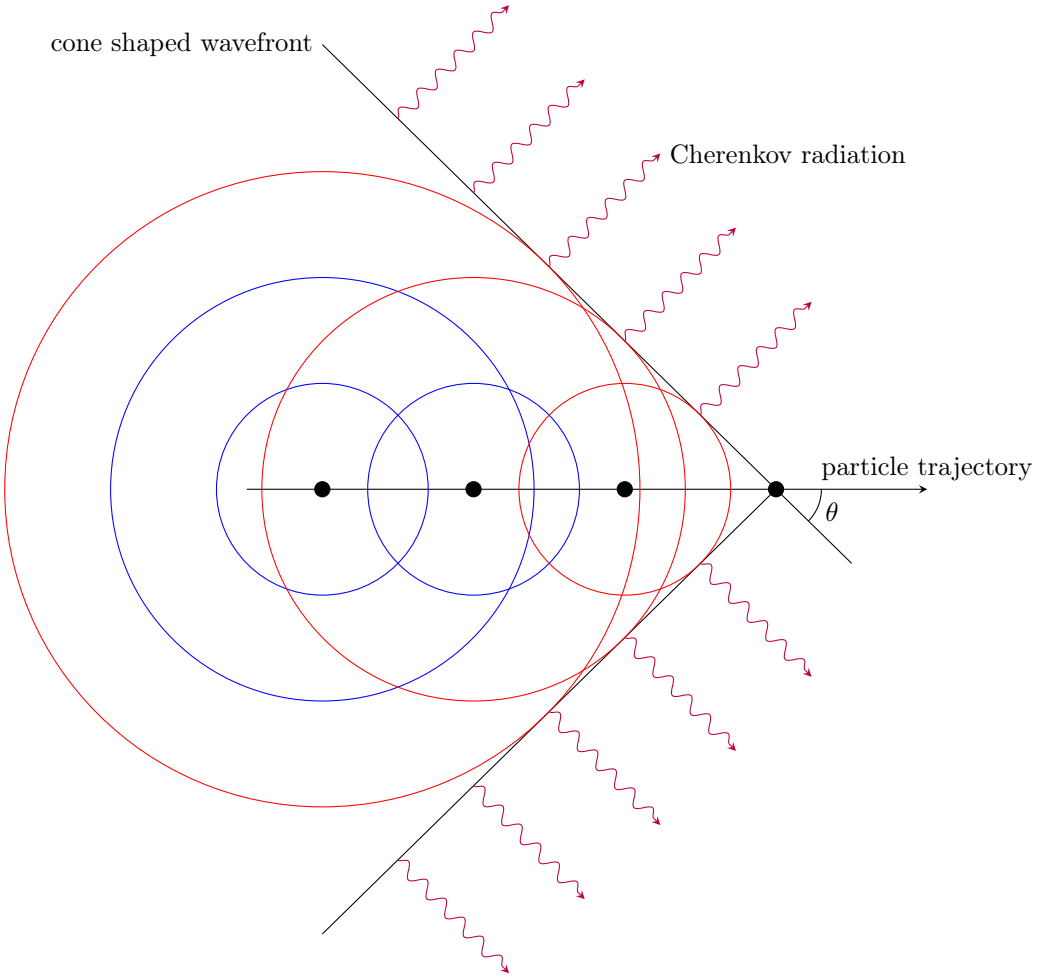

Figure 11: Illustration of the Cherenkov effect caused by a charged particle with velocity $v_{\text{particle}} > c_{\text{m}}$ in a dielectric material. The wavefront with the characteristic opening angle θ is created by the constructive superposition of the electromagnetic waves of the neighboring dipoles.

where a photon is generated by an electron during the avalanche and is then absorbed by an adjacent SPAD. This photon generates an electronic hole pair in the adjacent SPAD, which leads to an avalanche. Furthermore, a SPAD needs a certain cooling phase after a breakdown, which can last several hundred microseconds and thereby defines the maximum count rate. In addition, a SiPM has only a certain geometric fill factor due to the space requirement of electronic components, as well as a delimitation between the SPADs to keep the crosstalk as low as possible.

By generating a measurable electrical signal it is possible to detect single photons due to the avalanche generated by only one charge carrier. In Figure 12, a an example of an electronics schematic of a SiPM is shown. Due to their mentioned characteristics SiPMs can be considered as an alternative to conventional PMTs. In the field of combined medical imaging such as PET-MRT, SiPMs are the primary photo detector of choice, because of their insensitivity to magnetic fields.

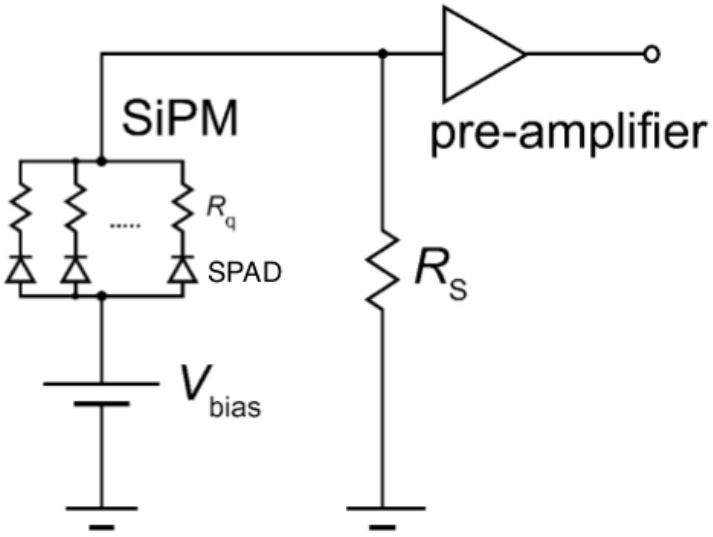

Figure 12: The simplified electronic layout of a SiPM [22]. The shunt resistor R_s converts the current of the SiPM into a voltage which is amplified by a pre-amplifier.

A special development of SiPM are so called digital SiPMs (dSiPM). Digital SiPMs combine the SiPM and dedicated readout electronics on one monolithic Si-chip. Dedicated electronics can, e.g. TDCs and photon counters or switches can be connected to each individual SPAD. Due to the possible early digitization of the signal, the device becomes, e.g. less sensitive to errors caused by electronics noise. E.g., a method of efficiently reducing the overall DCR is the possibility to disable individual SPADs with DCRs significantly higher than the average (so called screamers). After a photon is detected, the SPAD is resequenced by a quenching transistor and after readout it is recharged by recharge transistor and again sensitive [2]. In Figure 13 a schematic representation of a dSiPM for the case of the digital photon counter is sketched.

2.5.1 The digital photon counter developed by Philips

The digital photon counter developed by Philips (DPC) consists of 16 dies, which represents the smallest independent unit of the DPC (tile) and each of them is able to perform the data acquisition

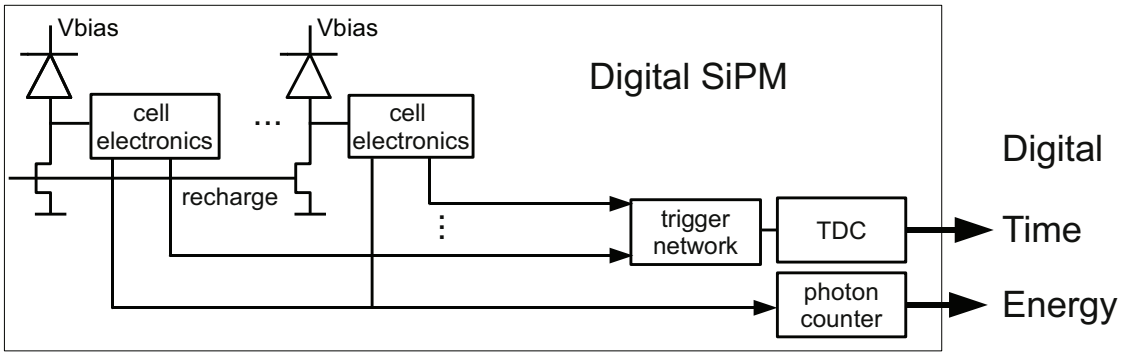

Figure 13: Structure of a dSiPM for optical photon detection systems [2].

and photon counting separately. Every die contains four pixels. Furthermore, each pixel consists of four sub-pixels which contain 3200 individual SPADs. The simplified structure of the DPC is shown in Figure 15. A SPAD is capable of detecting exact one (first) photon per acquisition. Therefor, the dynamic range per event and die is defined by the number of SPADs per die. Furthermore it is possible to configure the acquisition sequence, see Figure 14. The DPC is a digital silicon photomultiplier with a single photon time resolution of 101 ps FWHM (for the case of a DPC-pixel) [23]. The DPC has a photon detection efficiency and is due to how efficient the detector can detect optical photons in a certain spectrum. The higher the PDE, the higher is the probability of detecting an incident photon. Characteristics of the DPC are shown in Table 1.

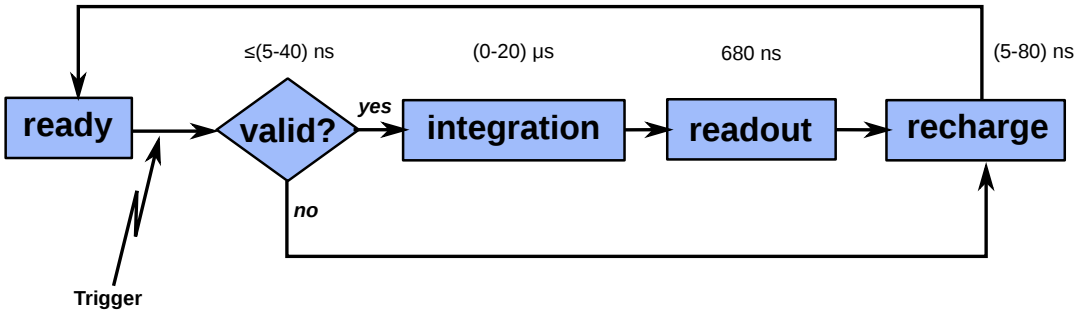

Figure 14: Process of an acquisition sequence for one event of a DPC developed by Philips [24].

Each Die has an independent trigger-network which triggers the acquisition sequence and defines the time of creating the timestamp [24]. Each individual SPAD has a trigger-line connected to a trigger-network, which again is connected to an on-chip TDC. The trigger-network can be set individually to a certain number of SPAD signals within a time frame which is necessary to start the TDC. If the TDC is not triggered within this frame (validation phase), the triggered SPADs are reseted. This can reduce the probability of releasing a false valid event by the DCR and keep the deadtime as low as possible.
In the case of a valid event, the TDC and the system starts with the integration phase. The detected photons on the individual SPADs are stored separately from the electronic cell. After the collection time the individual SPADs of the photon accumulator are read line by line in order to

prevent a high wattage at global recharge. Subsequently, the system (TDC, trigger network) is reseted to be sensitive again for the next event.

For an increasing number of simultaneously impinging photons, saturation effects increase due to the limited dynamic range (i.e. number of SPADs per die). This effect can be corrected by following equation:

$$p = N \ln\left(\frac{k}{N}\right). \tag{13}$$

p	number of incident photons corrected for the pixels photon detection efficiency
N	number of active SPADs
k	number of fired SPADs

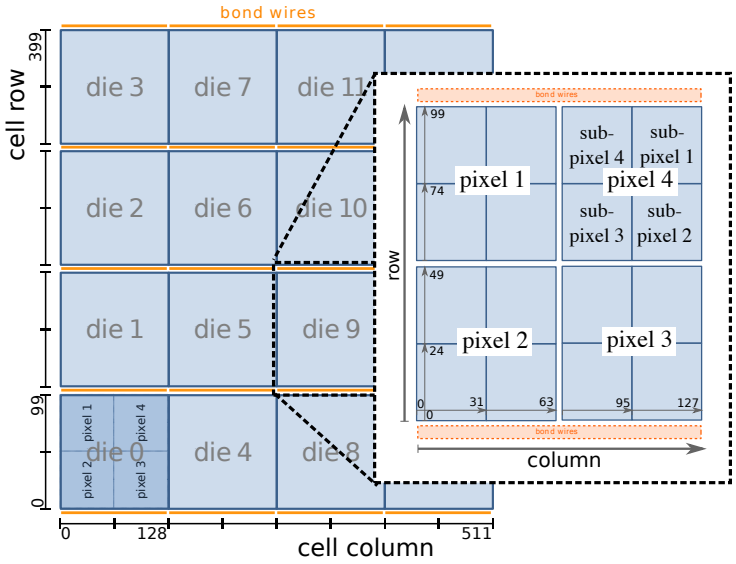

Figure 15: Schematic layout of a DPC tile [24].

2.5.2 Timing theory

The coincidence resolving time (CRT) is the detection time difference of the first detected optical photons caused by the correlating annihilation photons. In time-of-flight positron emission tomography (TOF-PET), the CRT is an important parameter for determining the location of the electron-positron annihilation which influences the signal-to-noise ratio during image reconstruction. The CRT depends on the resolving time of the detectors and the material dependent timing characteristics of the luminescent response to radiation. Currently, a CRT for SiPMs under laboratory conditions can be achieved in the range of 175 ps-330 ps FWHM can be achieved under laboratory conditions [25]. Due to the almost instantaneous emission of Cherenkov photons due to ionizing radiation, might be promising to use this radiation for improving the CRT. One disadvantage is the low light yield for Cherenkov radiation and the limited photon detection efficiency (PDE) of current detectors.

DPC-Tile	
Number of Dies (smallest independent DPC unit)	16 (4 x 4)
Outer Dimensions [mm]	32.6 x 32.6
Glassplate and Glue thickness (front side) [μm]	100 + 75
Fill Factor [%]	$\approx$ 74
DPC-Die	
Max. Event Rate	122 kcps
Dimensions [mm]	7.886 x 7.159
Number of Pixels	4 (2 x 2)
Active Pixel Area [mm]	3.8016 x 3.2
SPADs per Pixel	3200
SPAD Size [μm]	59.4 x 64

Table 1: Characteristics of the DPC developed by Philips [5].

2.5.2.1 Timing resolution of the DPC

In this sub-seciton the essential factors responsible for the timing resolution of radiation detectors for TOF-PET are described. In general, the timing resolution for dSiPM based scintillation detectors can be parameterized using the following equation,

$$TR(n) = \frac{p_0}{n^{p_1}} + p_2, \tag{14}$$

where n is the number of photons, p_0 is the time resolution relative to the system time resolution and p_1, p_2 represents the time resolution as a function of the number of photons [26].

For a high number of photons the time resolution $TR(n)$ converges asymptotically to the system time resolution, depending mainly on electronics jitter (time-pick-off jitter, jitter of the time-to-digital converter (TDC) and the clock jitter) which are limiting the time resolution. The time-pick-off jitter is due to noise, the TDC jitter is caused by electronic effects of the device and the clock jitter is caused by the distortion of the electric time pulse due to signal transmission to the DPC. As the resolution depends on the number of absorbed photons per avalanche per SPAD. Thus, the timing resolution of two SPADs which have absorbed a different number of photons in a period, increases. However, the time resolution is decreasing for a higher photon intensity with a minimum in the range of 10 to 100 photons per SPAD triggering, simultaneously. This effect can be explained by the increasing probability for fast breakdown. In a further increase of the photon intensity the time resolution increases again, but for that no explanation exists. A time resolution of 42 ps $\pm$ 0.8 ps FWHM with a Die as active area with 20 % inactive sells can be achieved under laboratory conditions [23]. It was observed that an increasing number of deactivated cells is improving the time resolution. This effect can be explained by the reduced influence of the trigger network skew as main part for a better resolution. The triggered network skew could be improved even better due to optimizing the detector architecture [23, 27].

After the influence of electronics on time resolution has been analyzed, the influence of the localization of the charge carrier injection and the statistical variation of the avalanche growth are discussed below. The structure of a SPAD is illustrated in Figure 16. The statistical fluctuation of

the avalanche growth is a significant limiting factor of the time resolution, which is influenced by the field strength distribution in the depletion layer. The spatial dilatation of an avalanche can be separated into three scenarios (scenario I - III in Figure 16). I Cascade generation of electron-hole pairs by the bias V_{bias} in longitudinal direction. II Diffraction of charge carriers in lateral direction. III During an avalanche a photon is generated and is reabsorbed in the depleted region and thereby causes a spatial distribution of the charge-carriers.

The location of the charge-carrier injection can also separated into three different cases (scenario IV - VI in Figure 16). IV the incident photon is absorbed at the edge of a SPAD and thus has a spatial limitation which slows down the avalanche growth. V absorption of a photon by photoelectric effect in the depletion zone which produces an immediate avalanche. VI absorption of a photon in the epitaxial layer. Thereby the excited electron has to diffuse into the depleted zone until it causes an avalanche [23].

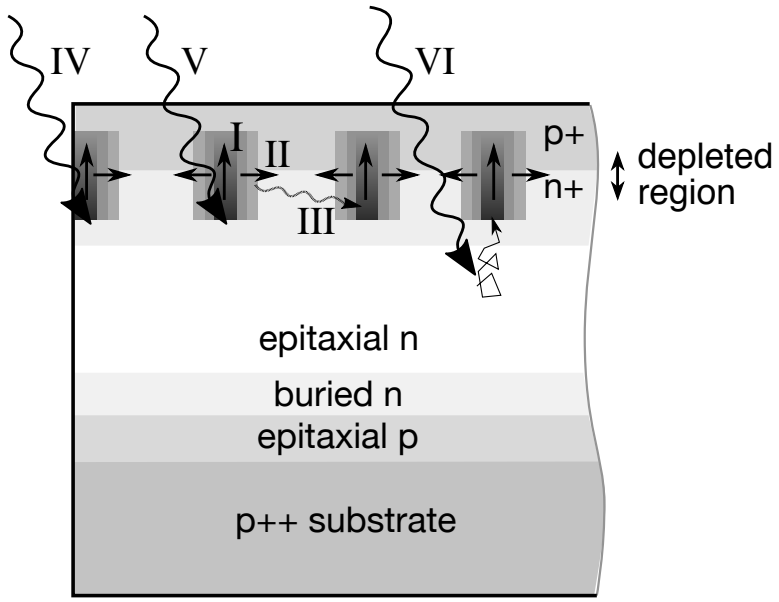

Figure 16: Schematic structure of a SPAD produced in CMOS technology [23]. Scenario I - III illustrates the spatial extension of an avalanche growth. Scenario IV - VI illustrates the different locations of a photon, absorbed by a photo electric effect.

2.5.2.2 Scintillation and Cherenkov radiation timing resolution

The time resolution of a detector convenient for TOF-PET is essentially dependent on the used scintillator crystal. In addition, there is the possibility to detect the Cherenkov light, emitted by the dipoles of a dielectric medium by a charged particle propagating faster than the speed of light in this medium, which is emitted almost immediately. A disadvantage is the low light yield of this radiation. The main causes for the timing distribution of the CRT due to the scintillator and the detected light will now be described in the following.

Among others, the time resolution of a scintillator based detector system depends on the photo electron density generated in the photon detector, emitted photon count, decay time, rise time,

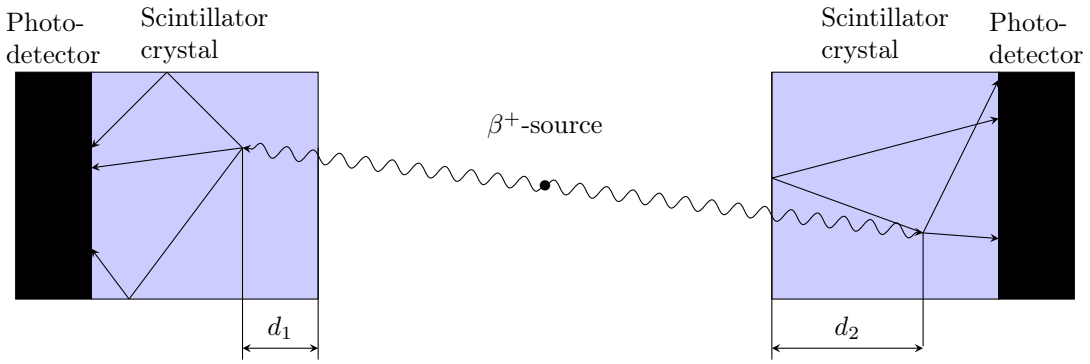

Figure 17: Illustration of the detection time difference of annihilation photons caused by different absorption positions in the scintillators.

surface properties, reflector properties, refractive index and the position of the photo electric absorption of the γ-photon in the detector. A reason for the degradation of the CRT is the propagation time in the scintillator crystal. Moreover, due to the different absorption positions of the two correlating 511 keV γ-photons as shown in Figure 17, a time difference results as propagation path length for optical photons is different. This results in a time difference

$$\Delta t = \frac{\Delta d(1-n)}{c}, \tag{15}$$

where $\Delta d = |d_1 - d_2|$ is the position difference, a is the crystal length and n is the refractive index of the scintillator. For this approximation it was assumed that the γ-photon and scintillation photon were emitted in both crystals perpendicular to the detector plane. A further worsening of the CRT is caused by an increasing average path length of the scinitillation photons increasing the crystal thickness.

A model, describing the possible CRT for a particular scintillator will be briefly discussed below. In general, there are some properties for a better time resolution: high light yield of the emitted photons, low decay time and low rise time. The emission of scintillation photons can be described by a bi-exponential function [28, 3],

$$p_{t_e}(t|\Theta) = \sum_i P_{ec,i} \frac{1}{(\tau_{d,i} - \tau_{r,i})} * \left[e^{-\frac{t-\Theta}{\tau_{d,i}}} - e^{-\frac{t-\Theta}{\tau_{r,i}}} \right]. \tag{16}$$

p_{t_e}	probability density function (PDF) of emitting scintillation photons at time t
Θ	absorption time of a γ-photon in the scintillator
$P_{ec,i}$	probability for the scintillation mechansim i which contributes to scintillation
$\tau_{d,i}$	decay time of the scintillation process i
$\tau_{r,i}$	rise time of the scintillation process i

The corresponding cumulative distribution function (CDF) is

$$P_{t_e}(t|\Theta) = \int_\Theta^t p_{t_e}(\hat{t}|\Theta) d\hat{t}. \tag{17}$$

Since there is currently no analytical description of the surface effects, crystal length, refractive

index to the photon detection timestamp, these effects are considered by the PDF $p_{t_{\text{trans}}}$ with transit time t_{trans} and σ_{trans}. This generalization by a PDF on the set T_N consisting of N discrete timestamps is possible due to the assumption of statistically independent and identically distributed photons. $p_{t_{\text{trans}}}$ is often approximated by a normal distribution. Therefore the PDF of the emitted scintillations photons can be written as

$$p_{t_n}(t|\Theta) = \int_0^{t-\Theta} p_{t_e}(t-\hat{t}|\Theta) \cdot p_{\text{trans}}(\hat{t}) d\hat{t}. \tag{18}$$

With the corresponding CDF,

$$P_{t_n}(t|\Theta) = \int_0^{t-\Theta} P_{t_e}(t-\hat{t}|\Theta) \cdot p_{\text{trans}}(\hat{t}) d\hat{t}. \tag{19}$$

For an ideal detector which is characterized by recording all timestamps for all detected photons and considering the order of detected photons, the PDF of the n^{th} of N photon results in

$$f_{(n)|N}(t|\Theta) = \binom{N}{n} \cdot n \cdot P_{t_n}(t|\Theta)^{n-1} \cdot (1 - P_{t_n}(t|\Theta))^{N-n} \cdot p_{t_n}(t|\Theta). \tag{20}$$

The PDFs $f_{(n)|N}(t|\Theta)$ of the first five and the tenth detected scintillation photons with a transit PDF, approximated by a Gaussian distribution with $\sigma_{\text{transit}} = 124\,\text{ps}$ [3] is shown in Figure 18a. LSO was assumed as scintillator crystal in the calculations. Figure 18b shows the probability density p_{t_n} of a LSO crystal with $\tau_{d,1} = 33.3\,\text{ns}$, $\tau_{d,2} = 7.1\,\text{ns}$, $\tau_r = 70\,\text{ps}$ and a yield-ratio of 0.07.

The lower bound for the best possible timing resolution which is constituted to the intrinsic timing resolution of a detector system, is theoretically given by Cramér-Rao lower bound, which is described as follows

$$var(\Xi|\Theta) \geq \frac{1}{I_{T_N}(\Theta)}, \tag{21}$$

with $I_N(\Theta)$ being the Fisher-information. For more information about the Fisher-information and the Cramér Rao lower bound, a reference is made to further literature [28, 29].

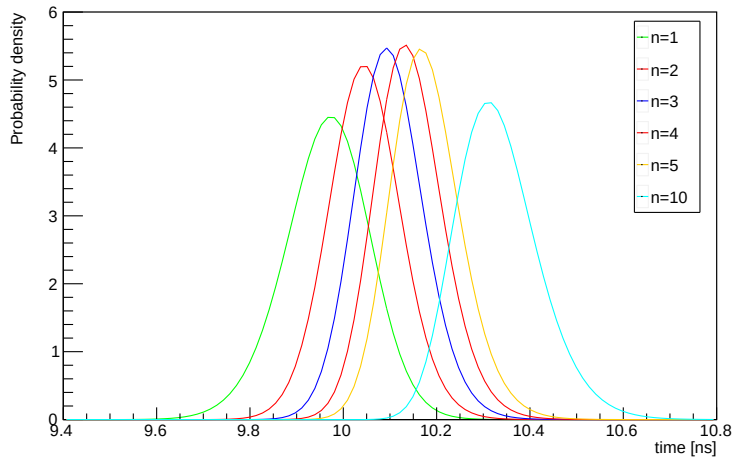

(a)

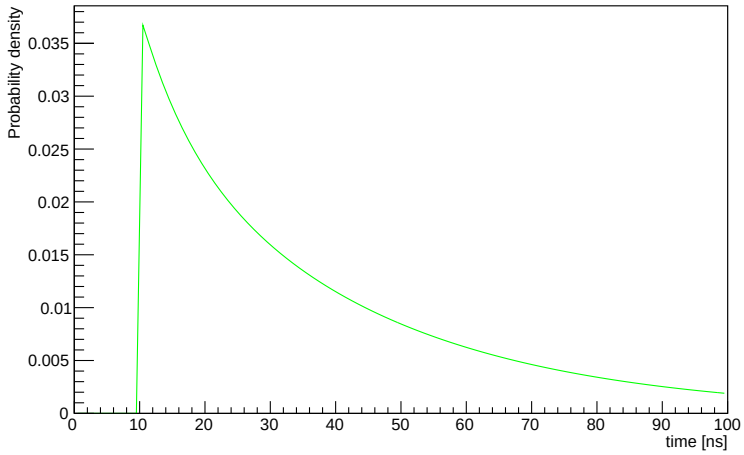

(b)

Figure 18: Figure (a) shows the probability density of the first five photons and the 10th Photon and Figure (b) shows the probability density p_n of a LSO scintillator crystal.

3 Experimentalsetup and analysis

In this section the experimental setup, which was simulated, as well as the used materials are described. The structural setup of the simulation, as well as the simulation data output, are explained as well. Towards the end of the chapter, the analysis of the data which were extracted by the simulation are discussed in more detail.

3.1 GEANT4 application

The GEANT4 application used in this work is based on the application developed in the course of a master thesis in the same field of research [5]. The simulation was developed further over the course of the work and adapted to answer a particular question. The data storage as well as

the detector construction were fundamentally changed related to the scintillator crystal dimension. The main focus in the simulation was the determination of the CRT calculated from correlating 511 keV annihilation photons and its dependence on the length and surface finish of the crystal. The surface between scintillator and reflector is simulated and compared with different simulation models provided by GEANT4. Furthermore, the detector-specific properties of the DPC such as time jitter, influence of deactivated SPADs (inhibit map), single photon resolving time, PDE and integration time, were considered in the analysis. In addition, the scintillator BSO was implemented in the simulation and compared with BGO.

All selectable parameters and their default values are listed in Table 2. The variable parameter of the detector geometry include the crystal length, scintillator material, scintillator configuration, number of DPCs and surface finish. The output and basic simulation parameter are controlled by the remaining selectable parameters such as TXT output, physics list, primary particle energy, GUI, event filter and number of good events.

Parameter	**Option**	**Range**	**Default Value**
Number of simulated Events	-nGoodEvents=N	$N \in [1, 10^{10}]$	500
Primary Particle Energy [keV]	-primaryE=T	$T \in \mathbb{R}$	511
Number of DPCs	-nDPC=N	$N \in [1, 2]$	1
GUI	-gui	[true, false]	false
TXT Output	-noTXT	[true, false]	false
Crystal length [mm]	-crystal_length=I	$I \in \mathbb{N}$	3
Event Filter	-singleInteractions -mDInteractions -allInteractions		-singleInteractions
Particle "Gun"	-pencilBeam -randomBeam -fanBeam_steps=N -fanBeam_xpos=X -pointSource	 $N \in \mathbb{N}$ $X \in \mathbb{R}$	-pencilBeam
Physics Builder	-stdEM_opt4 -physList_penelope -physList_livermore -physList_DNA -physList_lowEP		-stdEM_opt4
Readout Mode	-spad -title -sp -gammastats		-spad
Scintillator Material	-LYSO -BGO -BSO		-LYSO
Scintillator Configuration	-Array -singleCrystal		-singleCrystal
Surface Finish	-polished -ground		-polished

Table 2: List of selected parameters.

3.1.1 Detector geometry

For the user of GEANT4, the NIST database is available with predefined elements, elementary materials and various compounds. Furthermore, it is possible to combine arbitrary elements into a substance and define its density. Material properties, such as reflectivity and refractive index can be attributed to the materials. In the application, the "world" is the volume containing the complete simulation geometry and providing the relative coordinate system. For this simulation this volume was defined to be filled with air. The detector geometry, including the source of the 511 keV γ-quanta, the scintillators and the DPCs are defined in this volume. As reflector material, barium sulfates was used assuming a reflectivity of 99 %. In the simulation two possible scintillation configurations are selectable (array and single crystal as shown in Figure 19). In case of simulating a single crystal, the scintillator was covered with a 0.75 mm thick reflector layer on all sides, except the one facing the detector. If a ground surface was simulated, a 650 nm large air gap is created between the reflector and the scintillator. The used scintillator materials were composed through chemical composition of the respective elements and assigned to their physical properties.

The scintillation characteristics for BGO was taken from [30, 31]. The emission spectrum between 1.56 eV and 3.97 eV was taken from [32]. The refractive index was taken from [33]. Information about the emission intensity of BSO have been measured at Delft University of Technology. The refractive index between 1 eV and 3.1 eV was taken from [34]. The values ranging from 3.1 eV to 5 eV were extrapolated from these data.

The DPC consists of a stack of different materials which is included in the simulation. Starting from the scintillator side there is a layer of glass, which is applied to the SPADs with glue consisting of an acrylic based compound. The glue is assumed as pure acrylic, due to lack of detailed information. The photodetector consists of pure silicon in the simulation. The photodetector is placed on top of a circuit board consisting of a compound of Epoxy and SiO_2.

In Figure 19, a cross section of the detector structure with a single crystal on the left and array configuration on the right is shown. A scintillator array has 8 x 8 scintillator crystals with constant pitch which are merged with a reflecting material. The pixels of the DPC have a different pitch, which leads to an offset towards the active area of the DPC and the scintillator. Furthermore the single crystal is centered over a pixel with a base of 3 mm x 3 mm.

For both configurations, (single crystal or array, respectively), the detectors are placed at a distance of 10cm relative to the origin of the coordinate system. A DPC consists of 4 x 4 Dies, which again consist of 2 x 2 pixels. One pixel contains 2 x 2 sub-pixels and one sub-pixel consists of 32 x 25 SPADs. SPADs are not explicitly simulated. The fact if and when a SPAD was triggered was extracted from the position of the impinging photons on the detector surface, which was compared with the location of the SPADs.

In Figure 20 and 21, the detector in a single crystal configuration with (pink) and without (blue) reflector cladding and without the glass plate and glue to ensure a better overview is shown. The scintillator is centered over a pixel of the DPC.

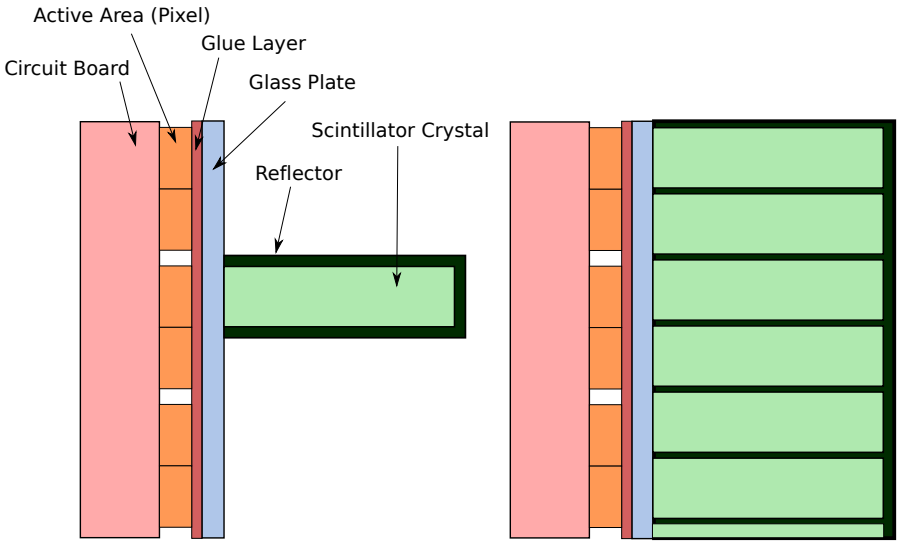

Figure 19: Detector cross-section of the simulated experimental setup. The left figure shows the single crystal configuration and the right figure illustrates the array configuration.

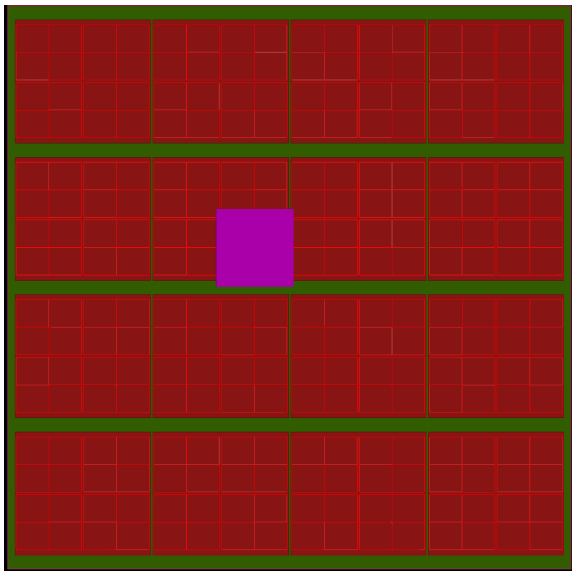

Figure 20: The single crystal configuration of the application is shown. Glass plate and glue are removed for a better overview. The smallest detector units which are shown are sub-pixels.

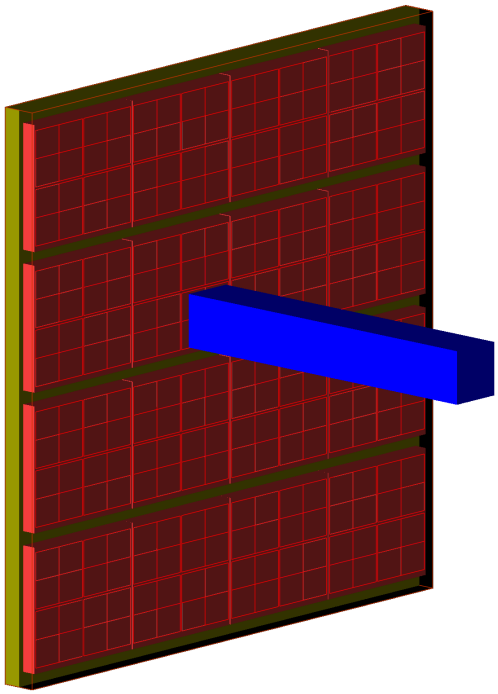

Figure 21: The single crystal configuration in angled view without reflector cladding is shown.

3.1.2 Particle source

The particle source in the simulation is located at the origin or offset from the origin on the X-axis, respectively, and creates 511 keV γ-photons with vertex to detector direction. Depending on which interactions are supposed to be simulated (all interactions, single interactions), the particle source emitts particles until the adjusted *nGoodEvents* are reached. Configurations of particle sources (so called particle guns) are listed in Table 2 and are explained in the following:

fanBeam_steps=*N*

Here, the particle source is moved N-times from the origin on the X-axis. N fan beams which are equidistant to each other are generated. Depending on which option (single crystal or array), the extension of the radiated region is either the scintillator crystal or the array block. For each position of fan beam nGoodEvents/N good events are generated. The fan beam is positioned in the YZ-plane and is normal to the X-axis. Figure 22 shows the configuration in the simulation.

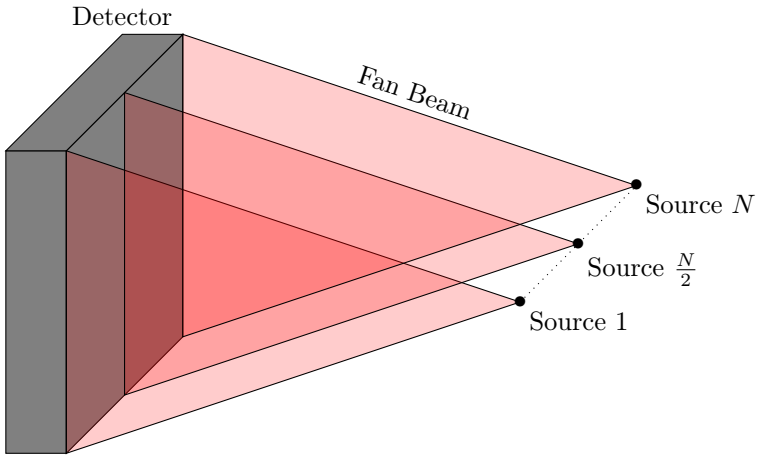

Figure 22: The fan beam N configuration is shown. The source is placed in the origin with N steps in X-direction per run. At the beginning the source is placed at the border of the detector. The offset per step is calculated as follows: Offset = detector width/N and per step *nGoodEvents*/N are simulated.

fanBeam_xpos=*N*

The beam source is located in the origin with an offset X, selected by the user, on the X-axis and irradiates the scintillator (single crystal) or the DPC (array) in the YZ-plane . Here, the position of the particle source is fixed for all events. Figure 23 shows the simulation construction.

pointSource

When a simulation of a single crystal is configured, the particle source is centered over the scintillator crystal in the XY-plane. In other configurations the particle gun is located in the origin. Back-to-back photons are generated pairwise. This means, that the first photon has a randomly created direction (depending on the set particle gun) towards the first detector, whereas the second annihilation photon has an inverse momentum compared to the first

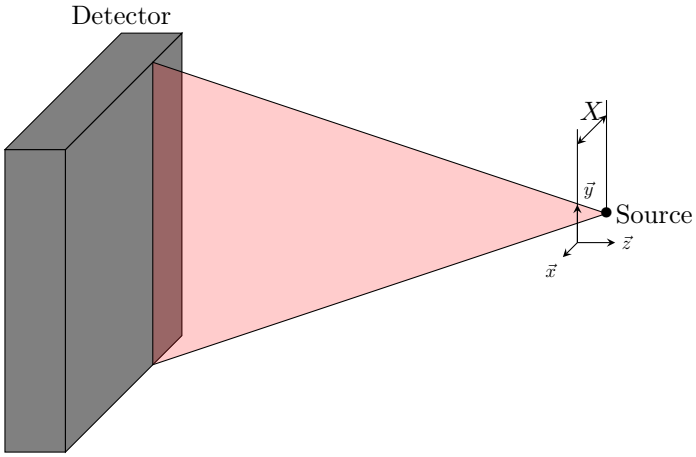

Figure 23: The fan Beam X configuration of the simulation is shown. The source position is placed in the origin with an offset X in X-direction. This position is fixed for the whole simulation. The photon beam direction is randomly distributed in Y-direction.

photon. The direction of the first photon is newly chosen for each created particle in the source. The interaction of the particles are evaluated until an event is evaluated as good. Only after that the second annihilation photon is created and simulated. In Figure 24 the setup in the simulation is shown.

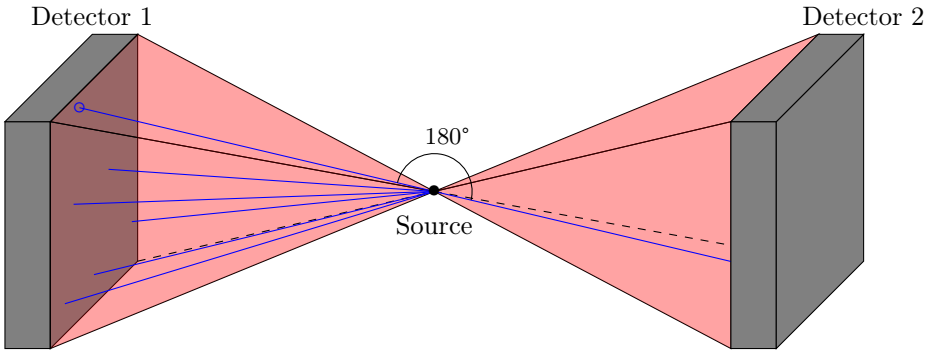

Figure 24: The point source configuration with a particle gun in the origin with back-to-back detectors is shown. In this illustration only the sixth photon reaches the detector (marked by the blue circle) gets detected by the first detector. The momentum of the photon is saved and rotated by 180 °(back-to-back). The next photons are "fired" in this direction until an event is counted as "good" by the application. Thereby only one line is drawn to the second detector.

pencilBeam

The particle source is located centered against the scintillator in the XY-plane, and emits photons in Z-direction. This type of source is used to cross-check the properties of 511 keV photons like mean free path length in a particular scintillator crystal. Thereby, comparisons between simulation and literature can be made, to review the implemented physics. In Figure 25 the simulation-setup is shown.

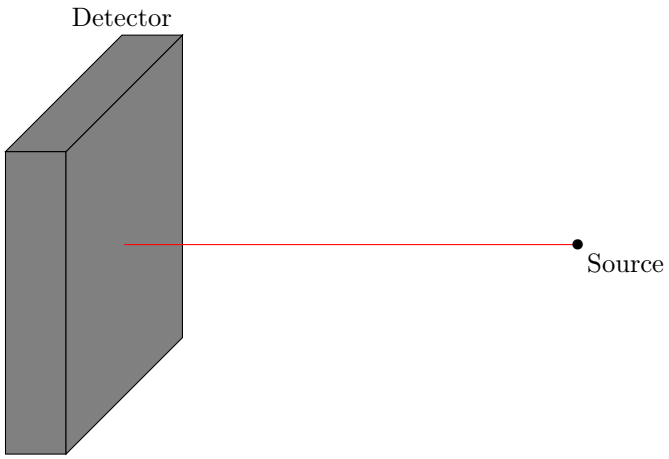

Figure 25: Shown is the pencil beam configuration in the simulation. The point source is placed centered over the scintillator and directs 511 keV photons in Z-direction.

3.1.3 Data aquisition and output

In GEANT4, The data of the simulation are generated in form of hits in GEANT4. A hit is recorded, if a physical interaction or an accumulation of interactions of tracks happens within the defined sensitive region. The definition of sensitive detector areas, which in a concrete example are scintillator, glass plate and sub-pixel, is important. The generated hit data, is stored in the Hits Collection.

Figure 26 shows the file structure which is generated by the application during a run. The structure of the folder name Sim Config # has a unequivocal declaration and is build with short variable names of the set simulation parameters: "PhysicsList _ParticleGun _EventFilter _NumberOf-SimulatedEvents _NumberOfDPCs _PrimaryParticleEnergy _ScintillatorMaterial _Scinitllator-Configuration _SurfaceFinish _CrystalLength". Due to stability problems of the simulation whose source has not been found yet, a trash folder is prepared. At the start of the run, the ROOT file is prepared in this folder. If the event is evaluated as "good" and the simulation processes until the end, the ROOT file is moved to the "root" folder. In this way, complications in the analysis are avoided. The created folders are constructed in a way, that different simulations with the same parameters are stored in the same folder. In this way, several simulations can calculate parallel, and thereby more events can be simulated faster. The respective, individually prepared filenames, are shown in Figures 27 and 28. It is also possible to prevent the generation of "* .txt" files with the option "-noTXT", in order to save space. All information which is included in the "*.txt" files, and more, is contained in the ROOT files and can be used for data analysis.

Before each event, six NTupels, are generated. An NTuple is a sequence of N elements of basic data types which may be manipulated in further processes. Its content is depicted in Figure 28. In the same the data structure of a "*.root" file, which is created during a run, is outlined. If an event of GEANT4 is classified as "good", the Hits Collection data are saved on the respective NTuples and are written into "*.txt" files. As depicted in Figure 27, one simulation and N-events files are created for each run.

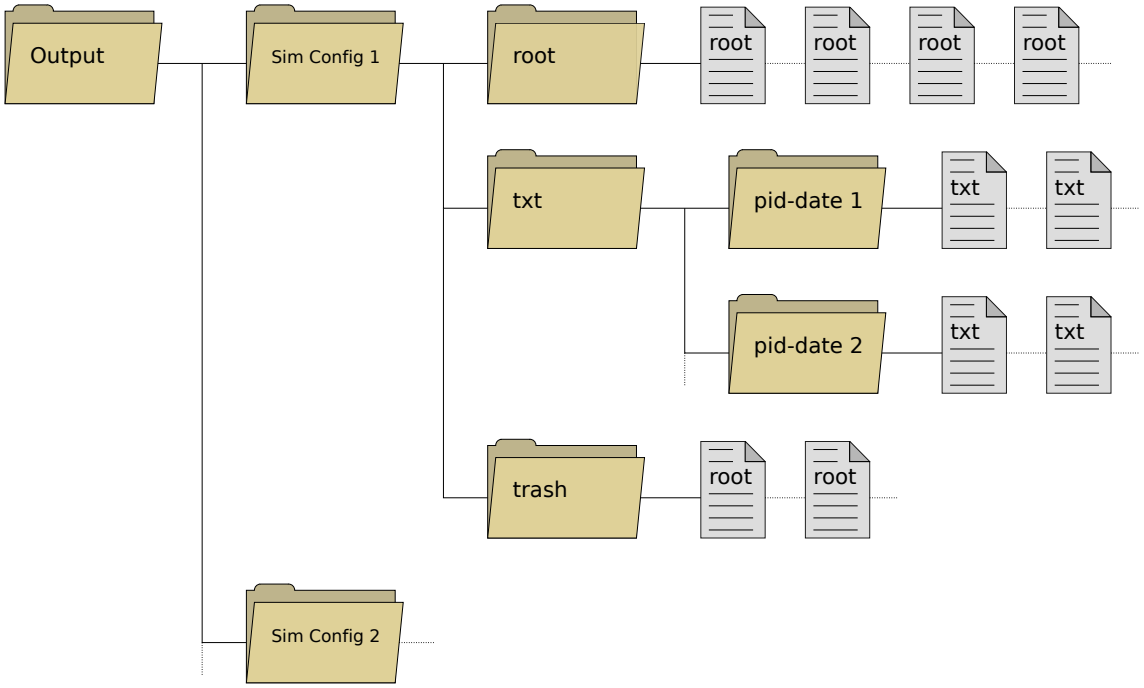

Figure 26: File structure created during a simulation.

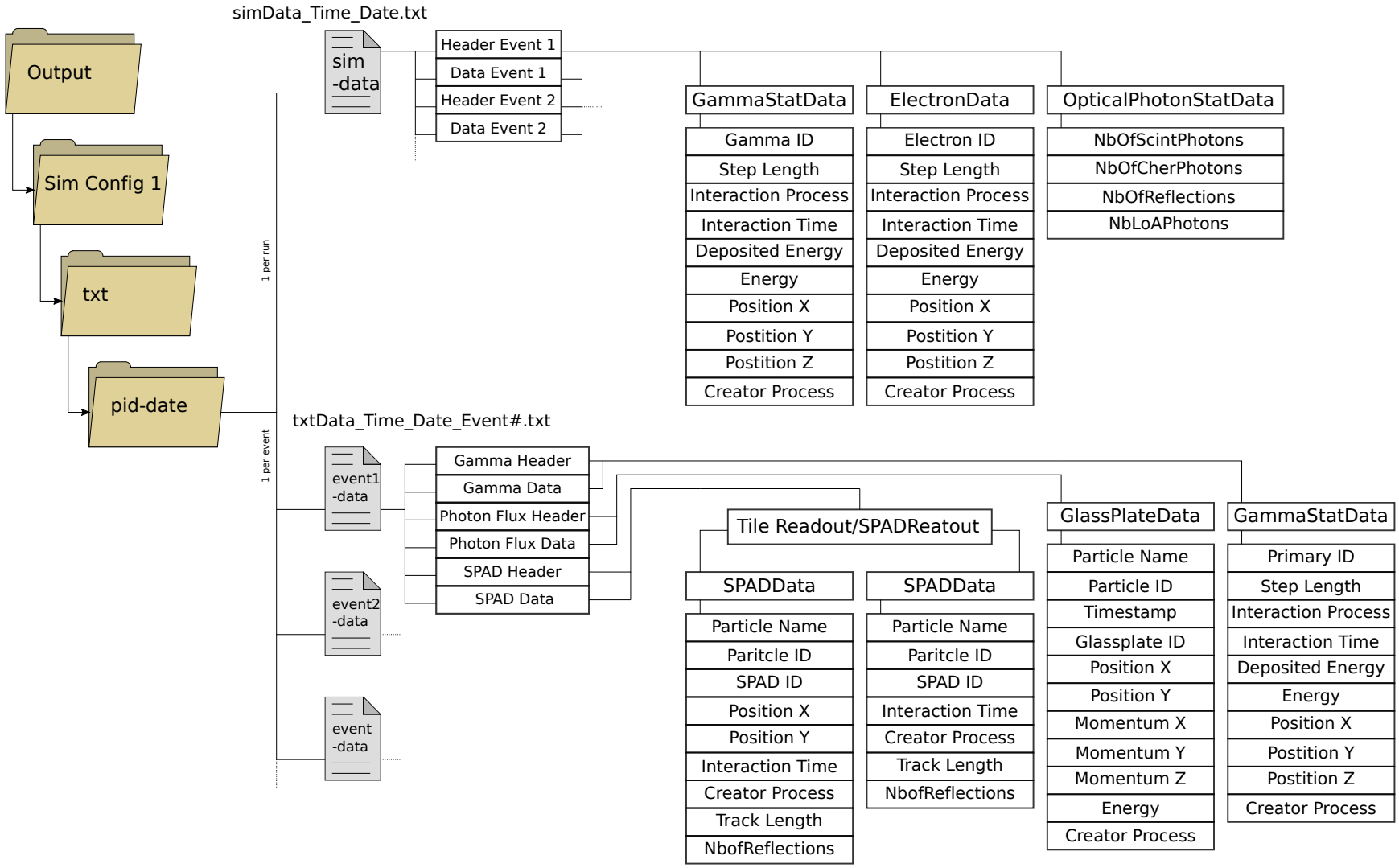

Figure 27: Structure of the created "*.txt" files per run. Each file consists of header and the corresponding files. The simData file is created at the beginning of a run an every good event writes the calculated data in the file and at the end of a run the file is closed. The txtData files are created and written only once per event and contain information about the γ-photons, created and detected optical photons.

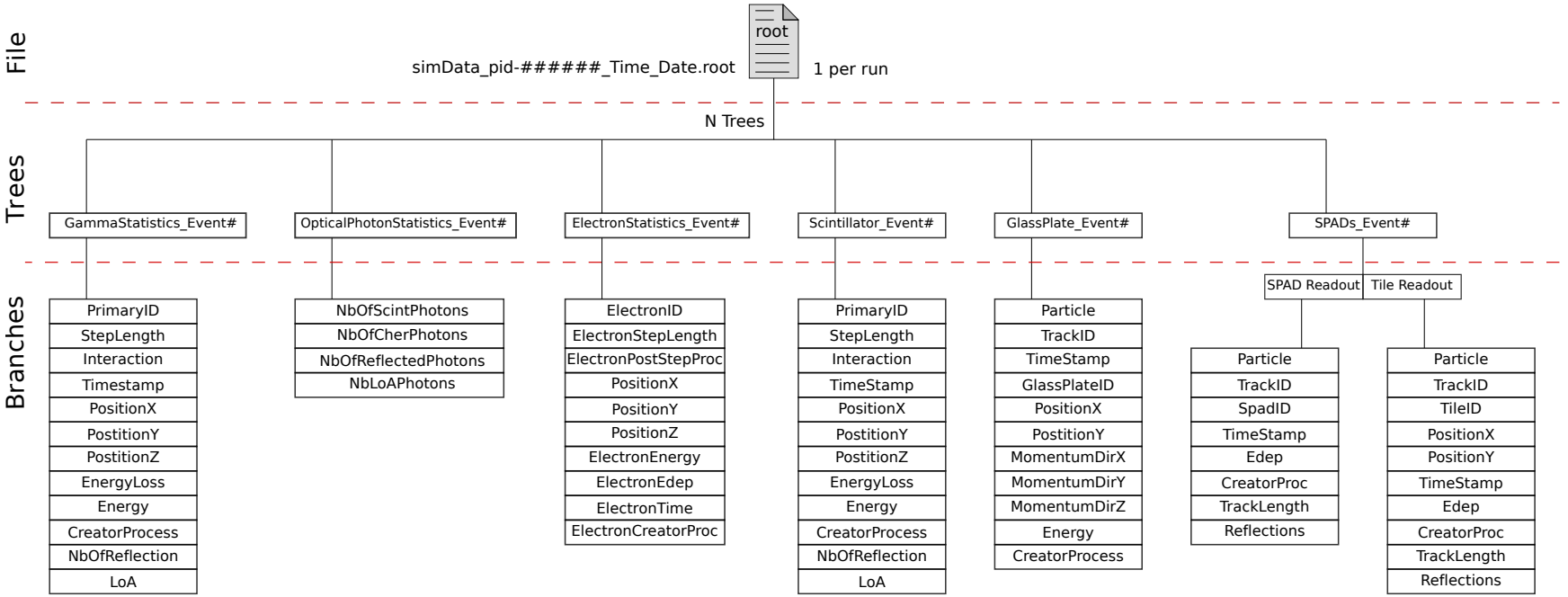

Figure 28: The structure of a ROOT file created per run is shown. The file contains n gamma statistics, optical photon statistics, electron statistics, scintillator, glass plate and SPAD trees corresponding to the n events per run. Each tree contains several branches with different information, e.g. gamma statistics contains only information about γ-photons created from the particle gun, bremsstrahlung and characteristic X-rays.

3.2 Data analysis

In the data analysis, the user has to state the directory, where the ROOT files which are supposed to be analyzed, are located. Afterwards, the files are opened, read in, and closed again. It turned out, that ROOT has unexpected problems with the simultaneous opening and closing of different files. The data structure is the same as shown in Figure 28. Depending on which plots are supposed to be created, data is used and edited by the respective functions. In Figure 29 the schematic process of the analysis of a simulation is shown in general. The direction of the arrows determines the information path or data transfer.

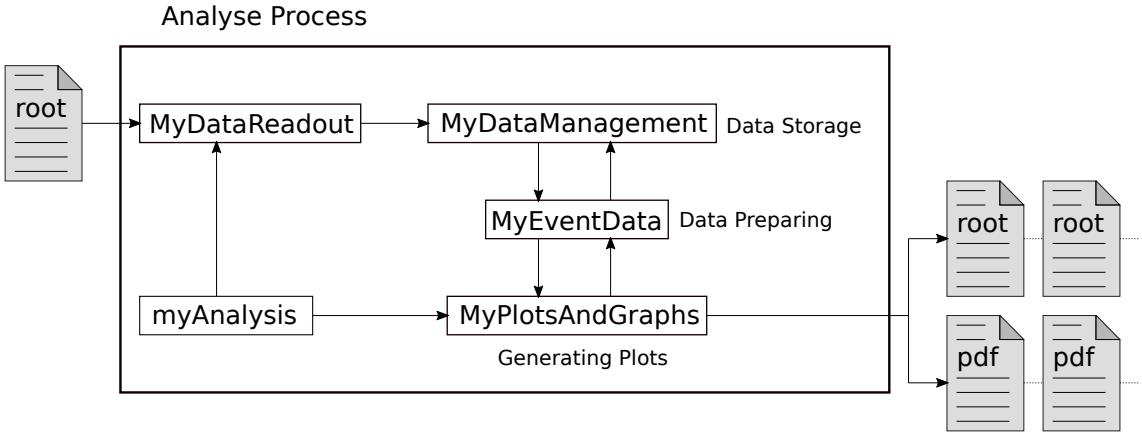

Figure 29: Schematic illustration of the process of the analyse application.

The data analysis of the simulation files, takes place over 5 stations starting from the data readout

MyDataReadout

The respective "* .root" files are searched, opened and written to the application's internal memory (MyDataManagement).

MyDataManagement

The structure of this class corresponds to the structure of a ROOT file as shown in Figure 28. There are 6 classes available which are written by MyDataReadout and read by MyEventData.

MyEventData

Evaluates simulation data retrieved from MyDataManagement for the respective plots. Detector properties such as single photon count, inhibit map, PDE and time jitter are considered here.

MyPlotsAndGraphs

Plots the simulation data, processed in MyEventData.

myAnalysis

Start of analysis, includes the main() function. The plots desired by the user, which are to be created in MyPlotsAndGraphs, are selected.

3.2.1 Analyse detection time

Detector-specific properties are considered in the analysis. These properties are the photon detection efficiency (PDE) [35] shown in Figure 30, the inhibit map, the single photon detection and the time jitter due to intrinsic time resolution of the detector. Each of these detector properties can be turned on and off in the analysis.

The inhibit map is an array of randomly selected SPAD IDs of a pixel, which are disabled. The number of disabled SPADs per pixel is indicated in %. If a photon hits such a SPAD it gets counted as not detected and is ignored in the following process. Due to fabrication defects and thermic caused avalanches some SPADs have a high DCR. To suppress this error, an inhibit map of disabled SPADs is generated.

In Figure 30, the PDE as a function of the wavelength is shown including the pixel-fill-factor of (74 % [35]). The selection whether a photon is ignored by the PDE or not, occurs randomly. For each photon energy, a specific PDE exists, which is selected for the respective photon in the analysis. A uniformly distributed random number is generated $\in [0, 1]$. If the generated number is smaller than the respective PDE, the photon is accepted.
In order to investigate the impact of the PDE on the coincidence timing performance, two artificial PDE distributions were simulated additionally and compared to the real one. On the one hand, UV-enhanced (PDE 0.4 between 400 nm - 269.53 nm) and on the other PDE 1 between 600 nm - 269.53 nm. Off this limits, the PDE measured by Philips was used.

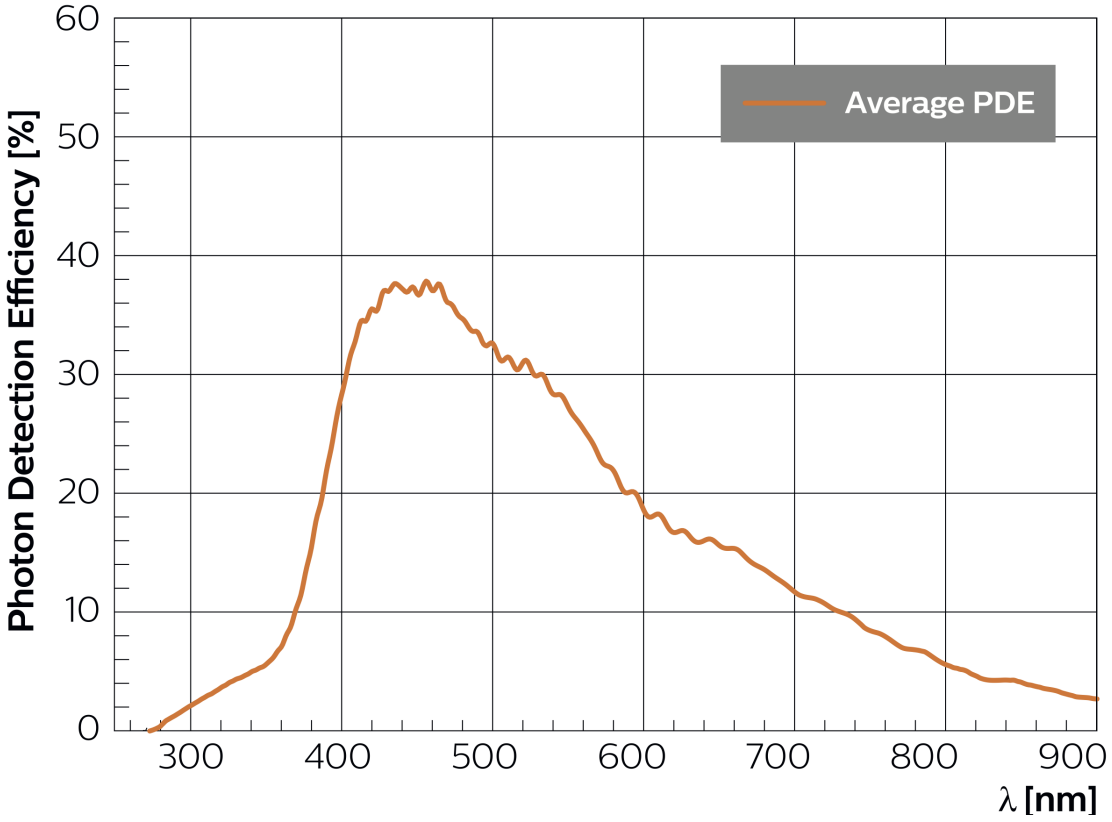

Figure 30: Typical photon detection efficiency of DPC3200-22-44 [35].

It is considered that individual SPADs during the integration time can only detect one photon which is further called SPDDIT (single photon detection during integration time). Therefor, all SPADs which had an avalanche during an event are saved and deactivated. Subsequent photons are therefor no longer detected.

The time jitter is included to the detection time of a detected photon and conforms to a random number of a Gauss distribution with standard deviation σ, with its mean being the initially simulated photon detection time and the σ the SPTR of the SPAD. Therefor, after adding the jitter, a new order of detected photons can occur.

Since in this work the analysis of the CRT for various parameter settings was a main task, the creation of the CRT in the analysis script is briefly explained in Figure 31. If the photon trigger level was assumed to be set to single photon, the CRT is given by the temporal difference of the first detected photons of the two detectors responding to the same coincident event. In the analysis the CRT dependent on the trigger level was investigated during the analysis, various detector properties like photon detection efficiency (PDE), inhibit map and time jitter are implemented. It is possible to activate or deactivate each detector property individually.

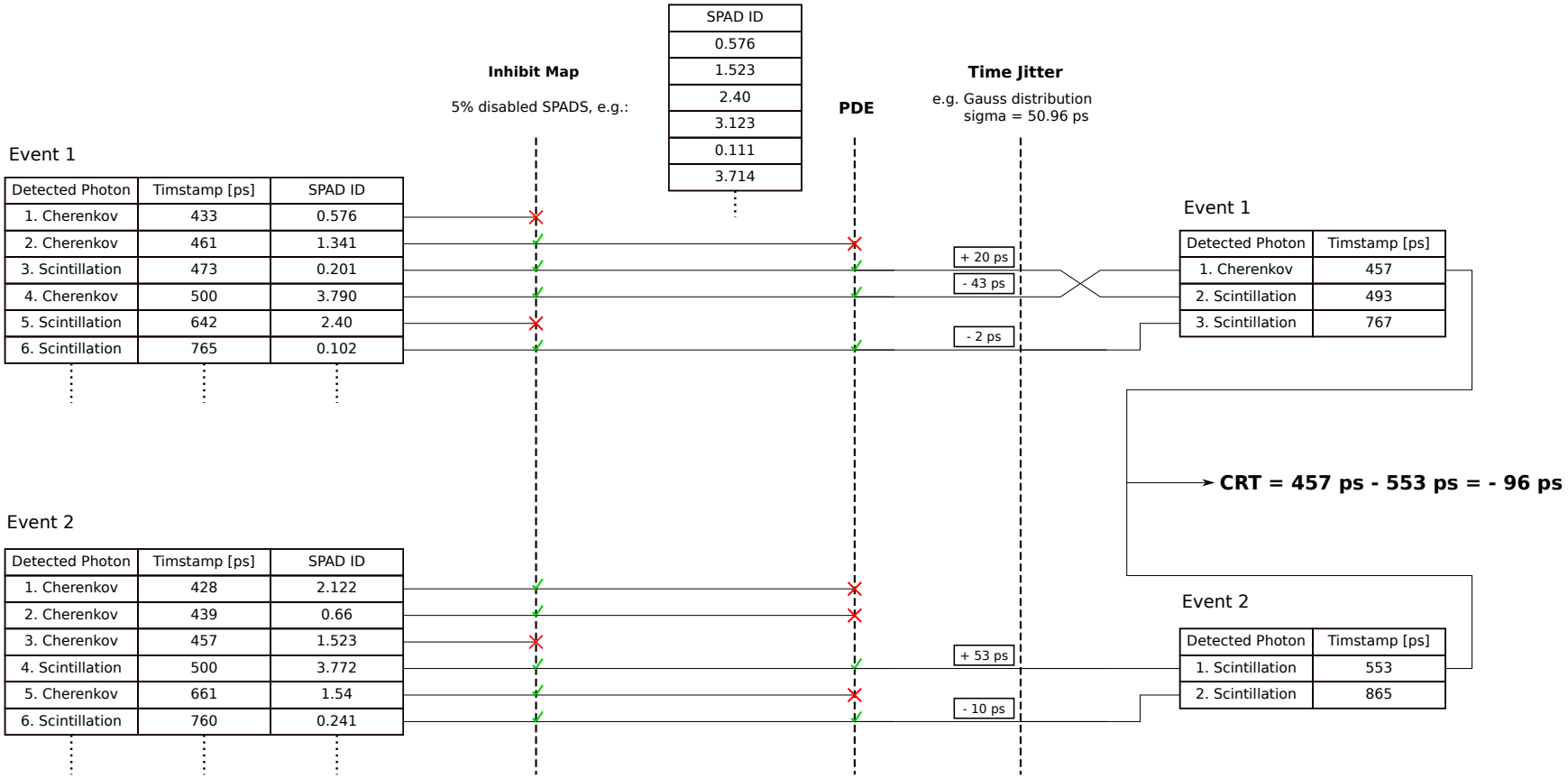

Figure 31: Example of a CRT calculation sequence including inhibit map, PDE and time jitter. The first six detected photons of the two correlating events are listed with timestamp and SPAD ID. At the beginning it is compared whether the photons have hit a disabled SPAD. If a photon hits a disabled SPAD it does not appear any further. After this it is calculated whether a photon is detected or not due to the PDE. Lastly, a time jitter is created based on a Gaussian distribution with a defined standard deviation $\sigma = 50.96\,\text{ps}$ [23] and added to the timestamp of the remaining photons. A new descending chronological sequence is defined, whereas the first detected photons form the CRT.

3.3 Scintillator materials

Bismuth Germanate ($Bi_4Ge_3O_{12}$, BGO) is a scintillating material produced since the 1960s [36]. BGO is frequently used for gamma ray detection because of its high density, high atomic number, cheap production, non-hygroscopity and high light efficiency. Due to the long decay time of BGO, the temporal resolution seems to be inhibiting its application in TOF-PET. Compared to other inorganic scintillators. The photoelectric absorption for γ-photons is high due to the high atomic number of the material. However, BGO provides a high refractive index, which is beneficial for the emission of Cherenkov radiation, the threshold for Cherenkov photon emission decreases with increasing refractive index.

Additionally, Bismuth Silicate ($Bi_4Si_3O_{12}$, BSO) was implemented into the simulation due to its shorter decay time, higher radiation hardness and low production cost compared to BGO [37].

In Table 3 some properties of BGO and BSO are listed.

BGO

Density [g cm^3]	Effective Atomic Number	Light Yield [phot.MeV^{-1}]	Decay Time [ns]	Cut-on Wavelength [nm]	Energy Resolution FWHM
7.13 [36]	75.2 [38]	8200 [30]	60 (10 %) 300 (90 %) [31] 85 (6.5 %) 370 (93.5 %) [39]	300	11.5 % [39]

BSO

Density [g cm^3]	Effective Atomic Number	Light Yield [phot.MeV^{-1}]	Decay Time [ns]	Cut-on Wavelength [nm]	Energy Resolution FWHM
6.8 [37]	-	1640 [37]	100 (100 %) [37]	300	22.2 % [37]

Table 3: Properties of BGO and BSO.

In Figure 32, the excitation, photo-luminescence, optical transmittance spectra of different heavy crystal scintillators and the theoretical limit of the transmittance for some heavy crystal scintillators are shown.

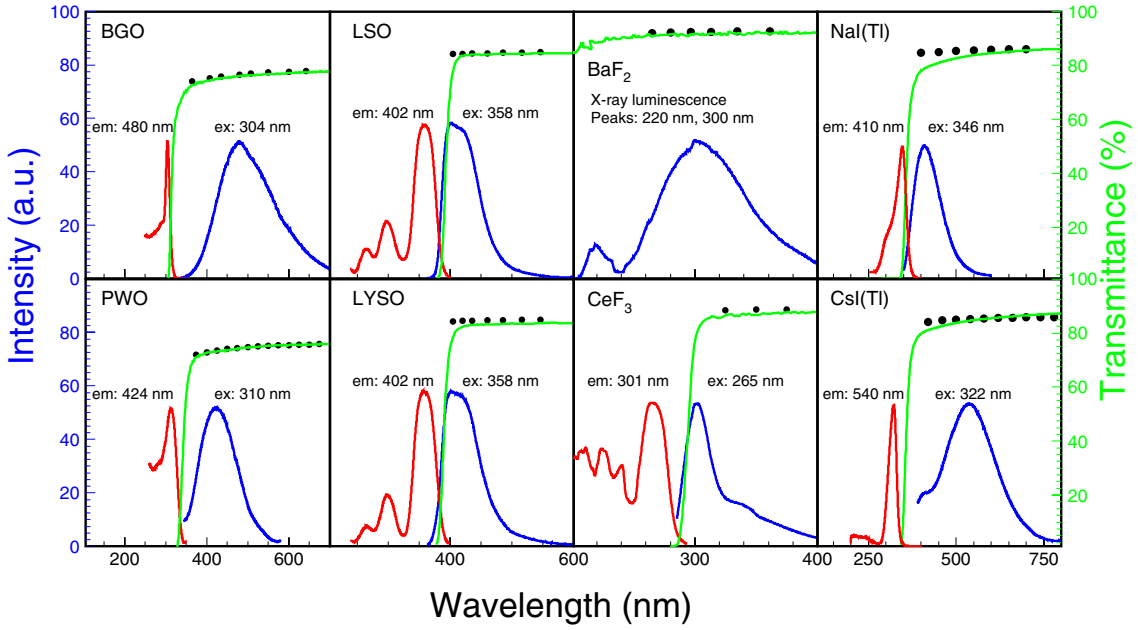

Figure 32: Shown are the excitation (red, created by a UV lamp and a monochromator), photoluminescence (blue), optical transmittance (green) and the theoretical limit of the transmittance (solid black dots) for heavy crystal scintillators. Figure copied from [32].

4 Results and discussion

At the beginning of this chapter, the theoretically predicted physical properties are tested. Furthermore, the temporal sequence of detected photons is analyzed separated, according to their creating mechanisms. After that, the coincidence resolving time is investigated, which is divided into two areas. On the one hand, the dependence of the CRT on surface properties and crystal length is examined, and on the other hand, the simulation data is compared with experimentally determined data. The simulation data is limited to the single crystal configuration.

4.1 Free path length of 511 keV gamma photons in BGO/BSO

The gamma free path length of the primary photon was simulated with a pencil beam (particle gun is centered and normal to the X-Y plane) with a high number (few millions) of events. The free path length is the length of an incident particle, from the entry in the matter, until its first interaction point. In Figure 33 and 34 the free path length for 511 keV photons in BGO and BSO is plotted. The fitting curve is a simple exponential function

$$f(x) = e^{p_0 + p_1 * x}. \tag{22}$$

$f(x)$	photon intensity function
p_0	simple constant
p_1	attenuation coeffiecient
x	depth of penetration

The attenuation coefficient for 511 keV annihilation photons in BGO and BSO was estimated using the NIST XCOM database [11] is $0.099\,035\,7\,\mathrm{mm}^{-1}$ for BGO and $0.099\,348\,\mathrm{mm}^{-1}$ for BSO. The calculated value from the simulation is $0.099\,741\,\mathrm{mm}^{-1}$ for BGO which is a relative error of 0.98 % and $0.100\,011\,\mathrm{mm}^{-1}$ for BSO which is a relative error of 0.67 %. These values correlate well with those of the literature. In Table 4, the relative proportions of 511 keV γ-photons, which interact in a scintillator crystal are listed for several crystal lengths. In this case, it must be taken into account that the particle gun emits the photons perpendicular to the XY-plane for the case of a pencil beam and thus, the length of the passage through the scintillator is limited by its length. For the case if a simulated point source the incident photons occur at a certain angle into the scintillator and thus have a variable interaction length (path through the scintillator). The probability that both annihilation photons interact in a scintillator crystal, corresponds to the multiplication of both individual interaction probabilities.

Crystal Length	3 mm	5 mm	8 mm	12 mm	20 mm
Interaction Probability BGO [%]	25.9	39.3	55	69.8	86.4
Interaction Probability BSO [%]	25.9	39.4	55.1	69.9	86.5

Table 4: The interaction probability of 511 keV γ-photons in BGO and BSO for different crystal lengths calculated with the simulated attenuation coefficient with a pencilBeam as particle source is shown.

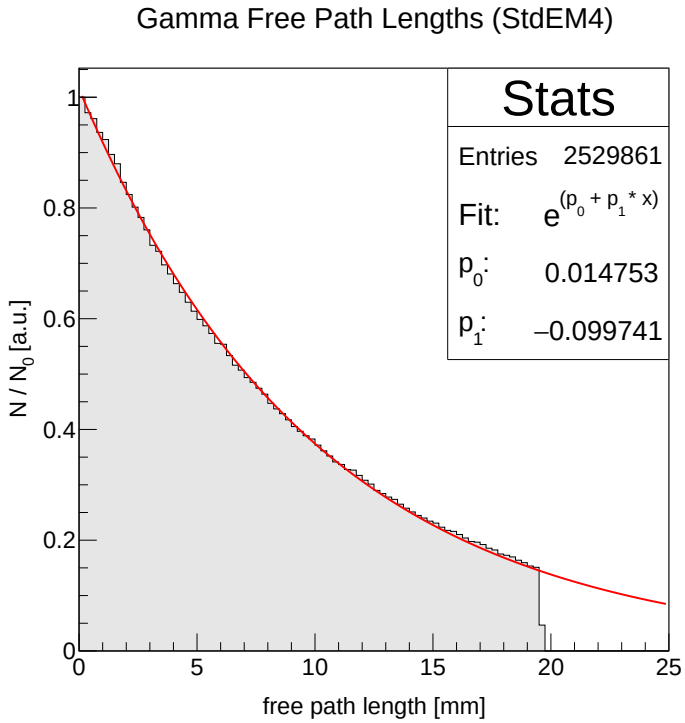

Figure 33: Free path length of 511 keV γ-photons simulated in BGO with a pencil beam.

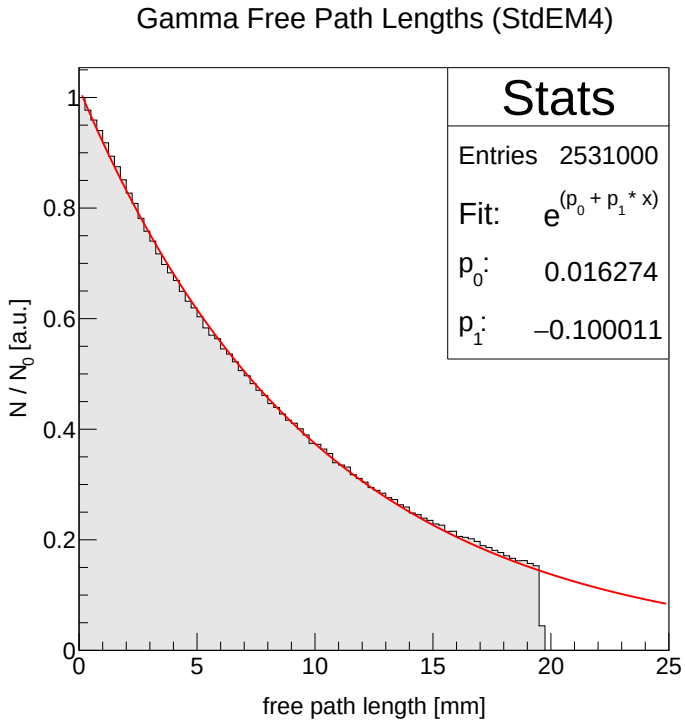

Figure 34: Free path length of 511 keV γ-photons simulated in BSO with a pencil beam.

4.2 Scintillation and Cherenkov energy spectra

The simulated scintillation and Cherenkov spectra are shown in Figure 35 and 36. Shown are the spectra for BGO, crystal length 20 mm, surface finish polished and single interaction (only photo electric absorption). The energy range depends on the in GEANT4 defined energy range of the refractive index (1240 - 248 nm), because only at this defined range, optical photons are simulated. The used values of the refractive index are obtained from the refractive index database [34].
The intensity of the Cherenkov emission decreases in the range of 354 - 310 nm in Figure 35 which can be explained by the decreasing transmittance towards the cut-off wavelength of 300nm. According to theory of radiation by moving chargers, the emission spectrum of Cherenkov photons should increase proportionally to λ^{-2} at the range of 1240 - 413 nm, but the number of emitted photons remains almost the same [40]. An explanation for this phenomenon is, that the increase of emitted photons is compensated by the reduction of the absorption length with increasing energy. For short wavelengths, the absorption length decreases further, which causes a negligible probability of detecting a higher-energetic photon.

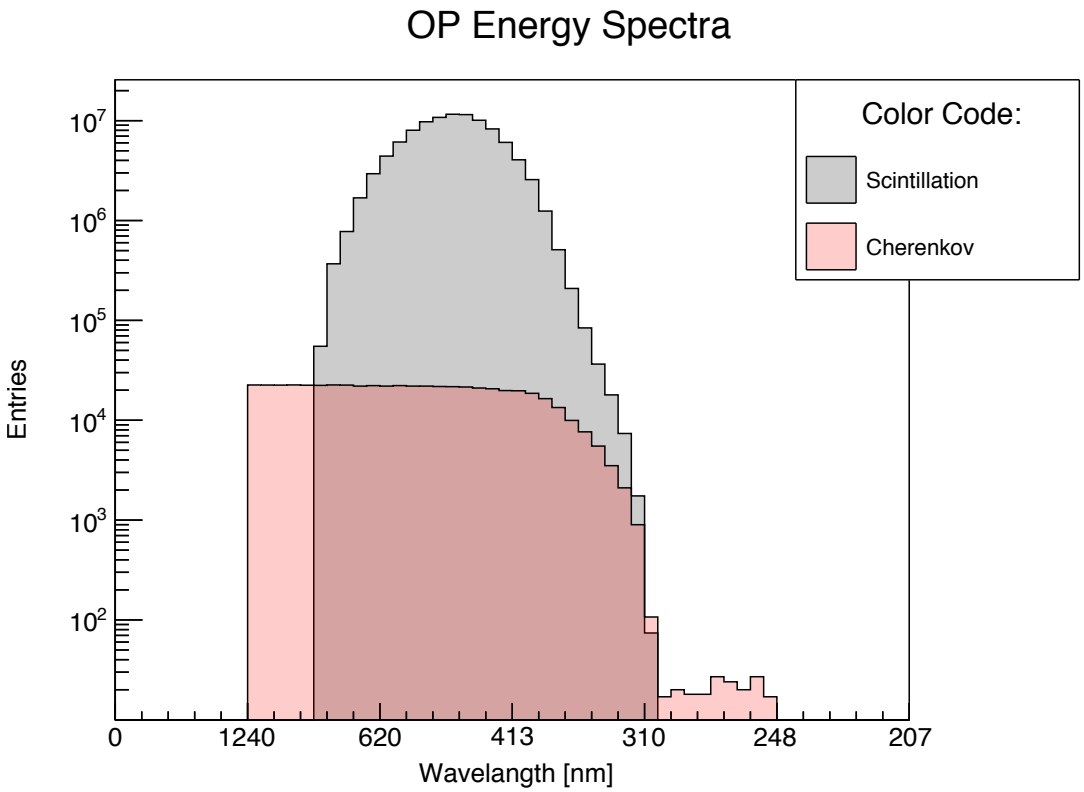

Figure 35: Optical Photon energy spectra defined between 1240 - 248 eV (definition range of the refractive index) of BGO, crystal length 20 mm, surface finish polished, single interaction (photoelectric absorption only).

In Figure 36, the same simulation data are is plotted, but including the characteristics of the photodetector (i.e. PDE, SPDDIT and inhibit map (5 % disabled SPADs) with PDE, SPDDIT and inhibit map (5 % disabled SPADs) is shown in Figure 36. Because the PDE is defined only in the

range of 900 - 273 nm, no photons are detected outside this energy range. As a result, the number of detected photons increases rapidly up to a maximum value (approximately 477 nm) which also corresponds approximately to the maximum of the PDE. When looking at higher energies the number of detected photons decreases rapidly, which is due to the shorter absorption length and lower PDE. The PDE of the DPC developed by Philips, shown in Figure 30, is used.

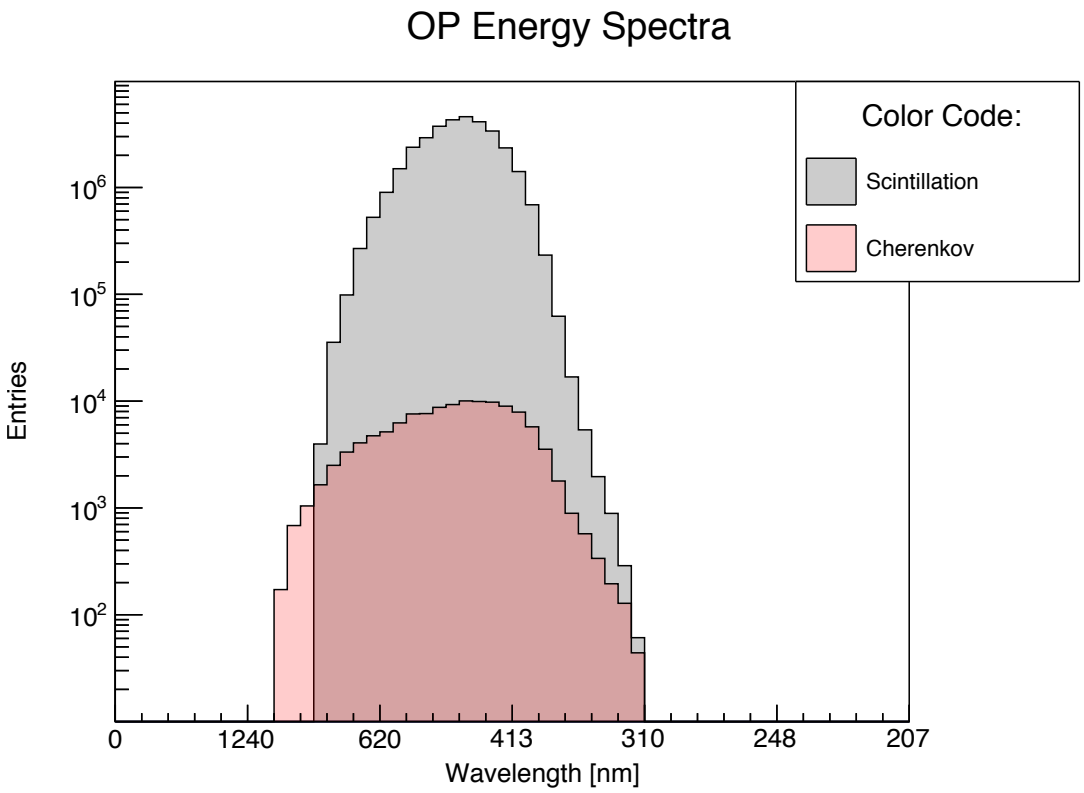

Figure 36: Optical Photon energy spectra defined between 1240 - 248 eV (refractive index definition range) of BGO, crystal length 20 mm, surface finish polished, single interaction (photoelectric absorption only) with PDE of the DPC, SPDDIT and 5 % inhibit map.

4.3 Optical photon statistics

In this section, distributions of various optical photon counts are discussed. For temporal reconstruction it is important to know how many Cherenkov and scintillation photons are created per valid event, how many of them are reflected in the scintillator, detected by the DPC and are lost or absorbed. An event is valid if the 511 keV annihilation photon was absorbed by the photoelectric effect in the scintillator. In Figure 37 various statistical photon count distributions are shown. The number of emitted scintillation photons created per event, are displayed in Figure 37a. On average, about 4,200 photons were generated, which is approximately half the light yield of BGO per MeV, which is expected for 511 keV gamma photons.

Figure 37b shows the number of created Cherenkov photons per event. Despite the low number of emitted Cherenkov photons per event, the first detected photon is mostly a Cherenkov photon due to the almost instantaneous emission. Thus, the Cherenkov effect is the predominant mechanism

for the temporal reconstruction of an annihilation event, which is created by the first detected photons.
In Figure 37c the distribution of photons which were reflected on a crystal surface at least once, are plotted. Due to the statistical treatment of reflections, reflected photons do not carry information about their origin anymore. It is obvious that the most emitted photons get reflected and thereby have a major influence on the temporal reconstruction of an event.
Figure 37d shows the absorbed and lost photons. An optical photon counts as lost or absorbed, when the photon is not detected in the logical volume of the SPAD (which means the photon is absorbed in the crystal, hits an insensitive part of the detector or leaves the crystal).
The distributions of detected scintillation and Cherenkov photons are shown in Figure 37e and 37f. It should be remembered that this two figures the PDE, SPDDIT, inhibit map and integration time of 128 ns are considered. This explains the significant difference between the number of created photons and the relatively low number of detected photons.

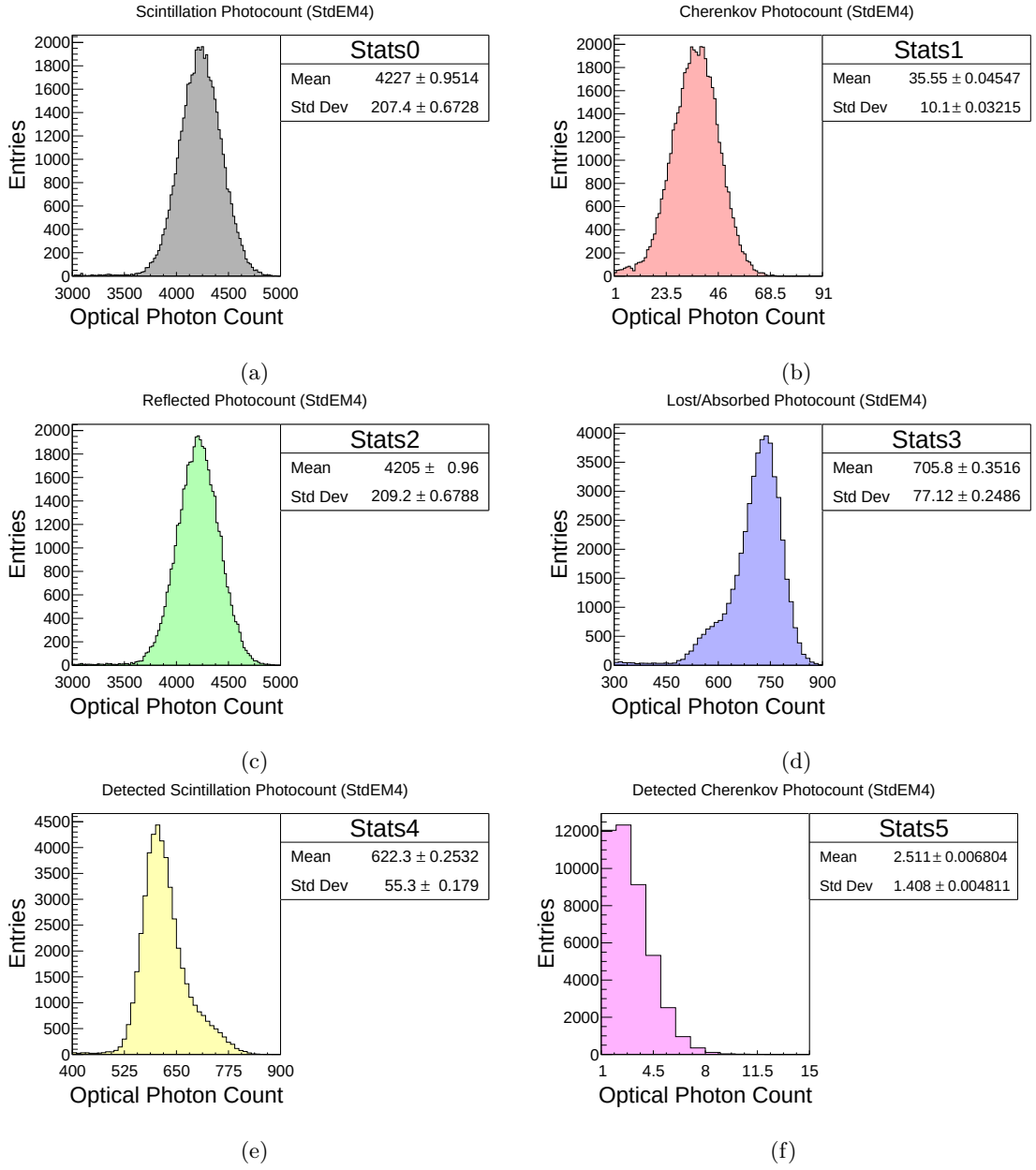

Figure 37: Optical photon count distribution for point source 511 keV γ-photon, single crystal 20 mm unpolished BGO scintillator material including PDE, SPDDIT, inhibit map and 1285 ns integration time. The x-axis illustrates the number of photons/event and the y-axis shows the number of events with a certain number of photons/event.

4.4 Detected photon count

In this chapter, the results of the number of detected photons simulated with the Glisur and LUT model provided by GEANT4 for an unpolished BGO scintillator crystal, are discussed. Due to the many degrees of freedom, the unified model was not examined in detail, since it would otherwise go beyond the scope of this thesis. Only events where all of the 511 keV were deposited to the scintillator by the photoelectric effect were taken into account. As described in Section 2.4.2, the

free parameters of the Glisur model are the reflectivity and surface roughness "polish" which can take values between $0-1$. In the LUT, the surface types "$polishedair$" and "$groundteflonair$" are used and the parameter σ_α is used to simulate the boundary layer scintillator air gap variations. Figure 38 compares the detected scintillation photon number for the different simulation models Glisur and LUT and different values of σ_α. Only scintillator finish type unpolished (ground), is shown in this figure, since a polished scintillator does not simulate an air gap between the scintillator and the reflector and thereby is simulated differentely.

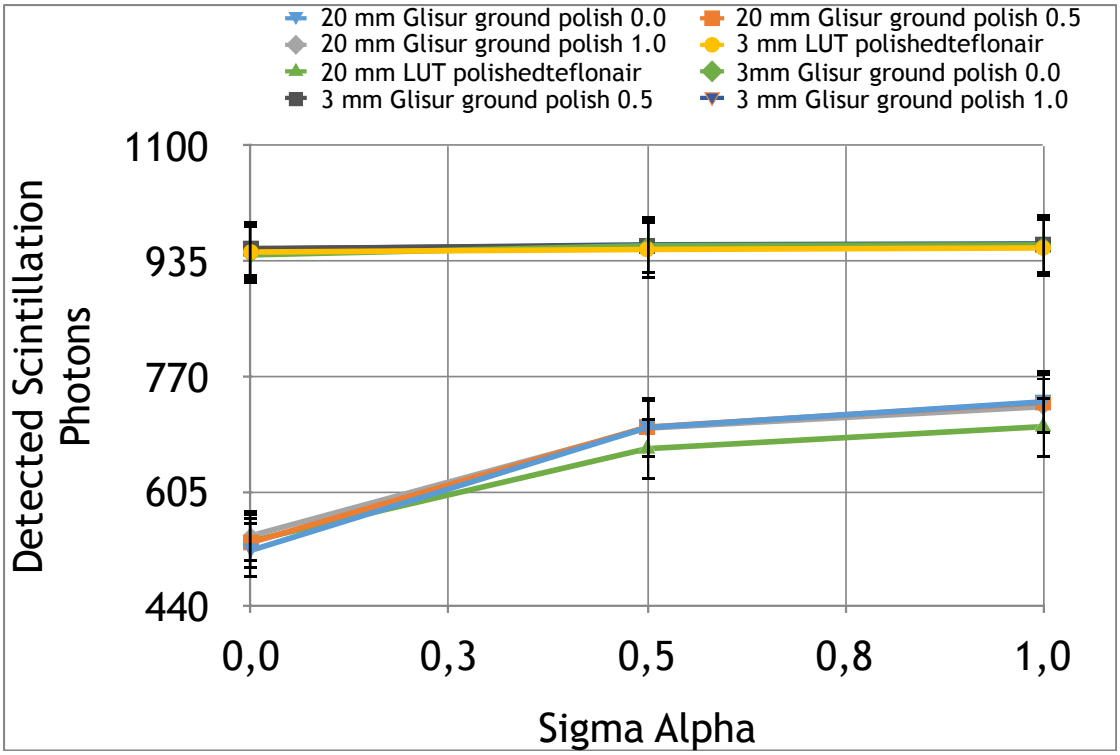

Figure 38: Mean number of detected photons of BGO as a function of the crystal surface roughness σ_α. The solid coloured lines are just to guide the eyes and are no interpolation of the diagram.

The PDE as well as SPDDIT and 5 % disabled SPADs were taken into account during the analysis. The integration validation times were adopted to compare the results with the values from [7]. The data from [7] correspond to the experimental realization of the simulation and are listed in Table 5. It can be seen that the results between the different models have no noticeable difference. Furthermore, no significant change is evident for a scintillator length of 3 mm with variable σ_α. The relative error for 3 mm crystal length is in the range 8.05 % - 9.55 %. The detected photon number for scintillator length 20 mm increases with increasing roughness and the relative error compared to the experimental value is in the range 0.02 % - 21.83 %.

The simulated photon count for BGO and BSO for different input parameter is listed in Table 6. The surface roughness for the unpolished scintillator was assumed with $\sigma_\alpha = 0.09$ rad and the reflector surface is simulated with the LUT "$polishedteflonair$". The detected photon count was separated into detected scintillations and Cherenkov photons. Only photons were considered, which were detected within the integration time. The relative error between simulation and experiment

Crystal Length [mm]	Surface Finish	Integration Time [ns]	Scintillator	Detected Photon Count [counts]	Standard Deviation
3	unpolished	645	BSO	279.15	22.55
20	unpolished	1285	BSO	161.10	14.63
3	polished	645	BSO	239.74	21.94
20	polished	1285	BSO	191.55	27.25
3	unpolished	645	BGO	1048.58	29.59
20	unpolished	645	BGO	669.4	26.9
3	polished	1285	BGO	788.1	30.55
20	polished	1285	BGO	520	26.4

Table 5: Experimental measured detected photon count of BGO and BSO with different scintillator length and surface finish [7].

Crystal Length [mm]	Surface Finish	Integration Time [ns]	Scintillator	Scintillation Photons	Std. Dev.	Cherenkov Photons	Std. Dev.	Relative Error [%]
3	ground	650	BGO	952.3	42.16	4.279	2.205	-8.77
20	ground	650	BGO	559	41.32	2.519	1.427	-16.12
3	polished	1285	BGO	947.1	42.31	3.862	2.039	20.67
20	polished	1285	BGO	689.7	38.21	2.772	1.538	33.17
3	ground	645	BSO	255.2	22.72	4.202	2.161	-7.07
20	ground	1285	BSO	138.7	18.03	2.459	1.393	-12.38
3	polished	645	BSO	229.4	21.38	3.804	2.007	-2.73
20	polished	1285	BSO	161.7	17.05	2.792	1.569	-14.13

Table 6: Simulated detected photon count separated in scintillation and Cherenkov photon count of BGO and BSO with different surface finish and crystal length. PDE, SPDDIT, inhibit map and integration time are considered.

ranges from 2.73 % - 33.17 %. For scintillators with unpolished surface, the error is between 7.07 % and 16.12 %, for polished surface it ranges from 2.73 % to 33.17 %. In general, the relative error for BSO is lower than for BGO. Furthermore, it can be seen that the detected Cherenkov photon number between BGO and BSO is approximately the same. This corresponds to the expectations due to the similar refraction index of both materials.

4.5 Photon arrival time

The photon arrival time (PAT) corresponds to the time difference of the γ-photon absorption time and the detection time of the individual optical photon. It can be differentiated between the two optical photon creation mechanisms scintillation and Cherenkov effect. Figure 39 shows the PAT of the first, tenth, and twentieth detected photon of a 3 x 3 x 3 mm^3 polished BGO scintillator. Figures 39a, 39c and 39e correspond to the PAT without PDE, time jitter, inhibit map and SPDDIT. The remaining three figures show the corresponding PAT when PDE, time jitter, inhibit map and SPDDIT. It can be seen that the average detection time and detected scintillation photons to total detected photons increases with higher photon number and with the

implementation of the detector properties. The PAT with detector properties has an expanded distribution, compared to the PAT without properties. When looking at the first arriving photons, Cherenkov emission is the dominant mechanism of the PAT, but it decreases rapidly with detector properties. Figure 40 shows the ratio detected Cherenkov photons to overall detected photons of the first 20 detected photons of a high number of events. Figure 40a shows the Cherenkov ratio for BGO 3 x 3 x 3 mm^3 polished and Figure 40b the one of BGO 3 x 3 x 20 mm^3 polished. For a 3 mm long crystal the scintillation creation process is dominant (detected Cherenkov photons/detected overall Photons ratio below 50 %) even for a threshold set to the 4th detected photon, while when detector characteristics is not included it is the threshold of 18 photons for a crystal length of 3 mm. For a 20 mm long crystal, the Cherenkov photon ratio below 50 % is noticed for the 3^{rd} photon with and the 10^{th} photon when not including detector characteristics.

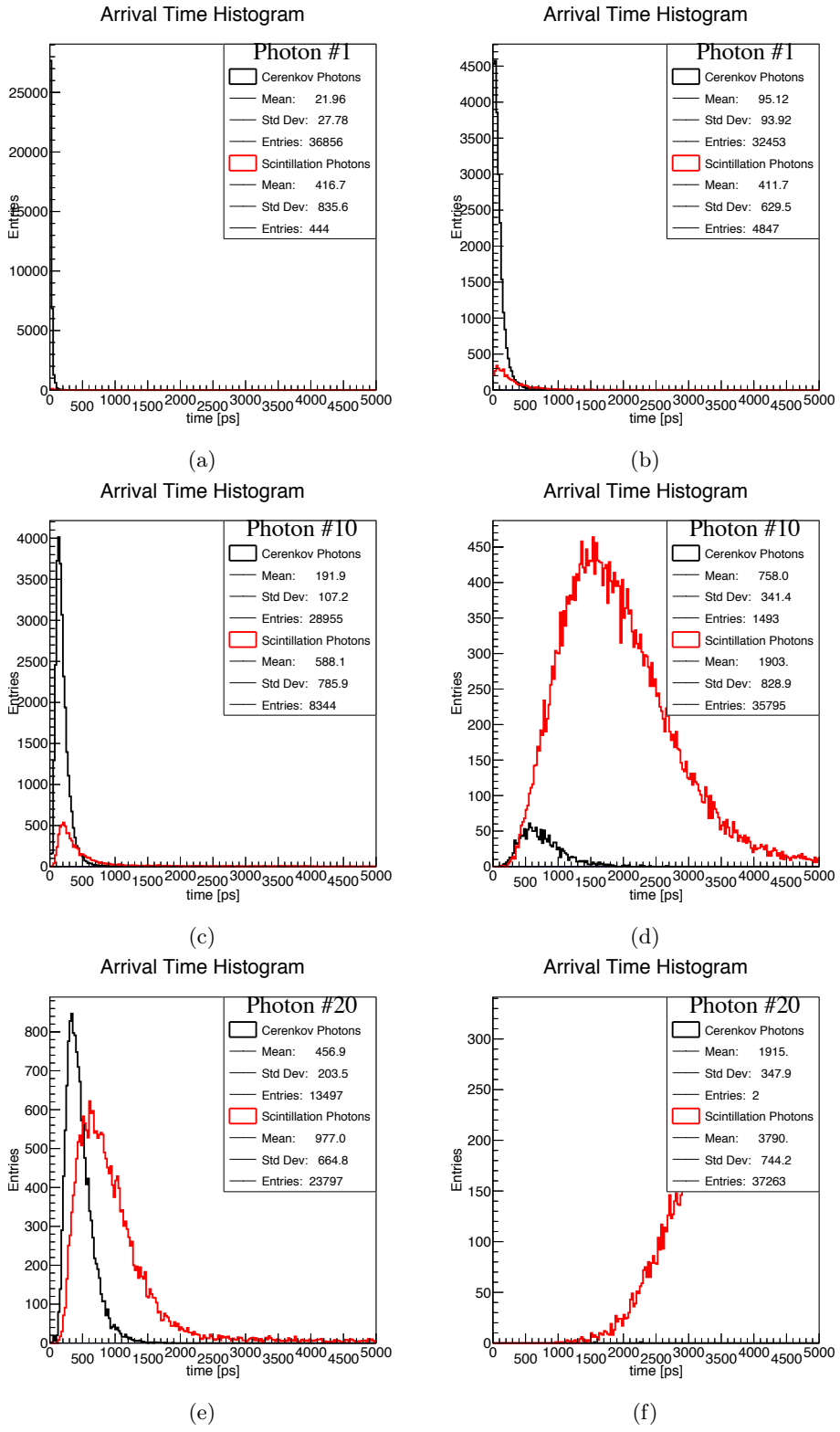

Figure 39: Photon arrival time of the 1st, 10th and 20th photon for BGO 3 x 3 x 3 mm^3 polished. The three figures on the left are without and the three figures on the right are including PDE, SPDDIT, inhibit map and time jitter.

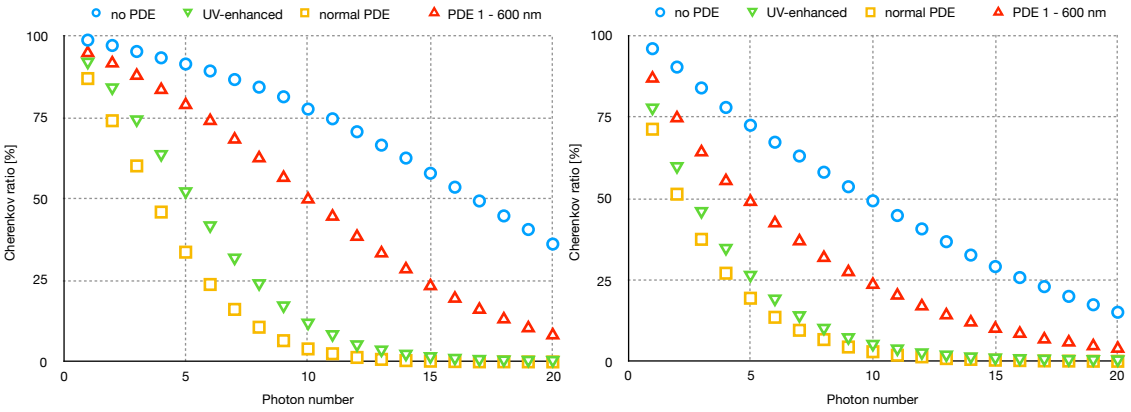

Figure 40: The detected Cherenkov ratio of the first twenty detected photons for BGO polished (a) 3 x 3 x 3 mm^3 and (b) 3 x 3 x 20 mm^3 with different PDEs is shown.

4.6 Coincidence resolving time

In the first part of this section, the dependence of the CRT on surface properties and crystal length is examined and in the second part the simulation data is compared with experimental determined data [7]. The CRT depends on many factors, such as scintillator material, crystal length, surface texture, PDE and the detectors time jitter. Measurements were made by a working group at TU Delft to determine the roughness of the unpolished scintillator, which gave an average value of $\sigma_\alpha = 0.09\,\mathrm{rad}$. All following simulated and analyzed data were performed with this roughness for unpolished scintillators. For polished scintillators no parameter had to be set.

In Figure 41 the CRT for a 3 x 3 x 20 mm^3 BGO scintillator crystal with surface finish polished, and reflector material teflon is shown. Only events in which both annihilation photons were absorbed by the photoelectric effect in the scintillator were taken into account. The top three figures from the left show the CRT with PDE from the Philips datasheet [35], PDE 0.4 from 270 - 400 nm and PDE 1 from 270 - 600 nm the detector time jitter. The same simulation parameters, only without time jitter are shown in the figures below. In these plots, the CRT is drawn for the individual creation mechanisms of the photons which are arriving first at the photodetector: Scintillation - Scintillation (S-S), Scintillation - Cherenkov (and Cherenkov - Scintillation) (S-C, C-S) und Cherenkov - Cherenkov (C-C). This is due to the almost immediate emission of the photons. The relative C-C ratio increases with improving PDE.
In Table 7, the ratio of the optical photon creation mechanism calculated with the PAT as shown in Figure 40 and the simulated ratio as shown in Figure 40 are compared. The probability that both of the first detected photons are Cherenkov photons calculated with the PAT, corresponds to the square of the Cherenkov ratio of the first detected photon, as shown in Figure 40b.

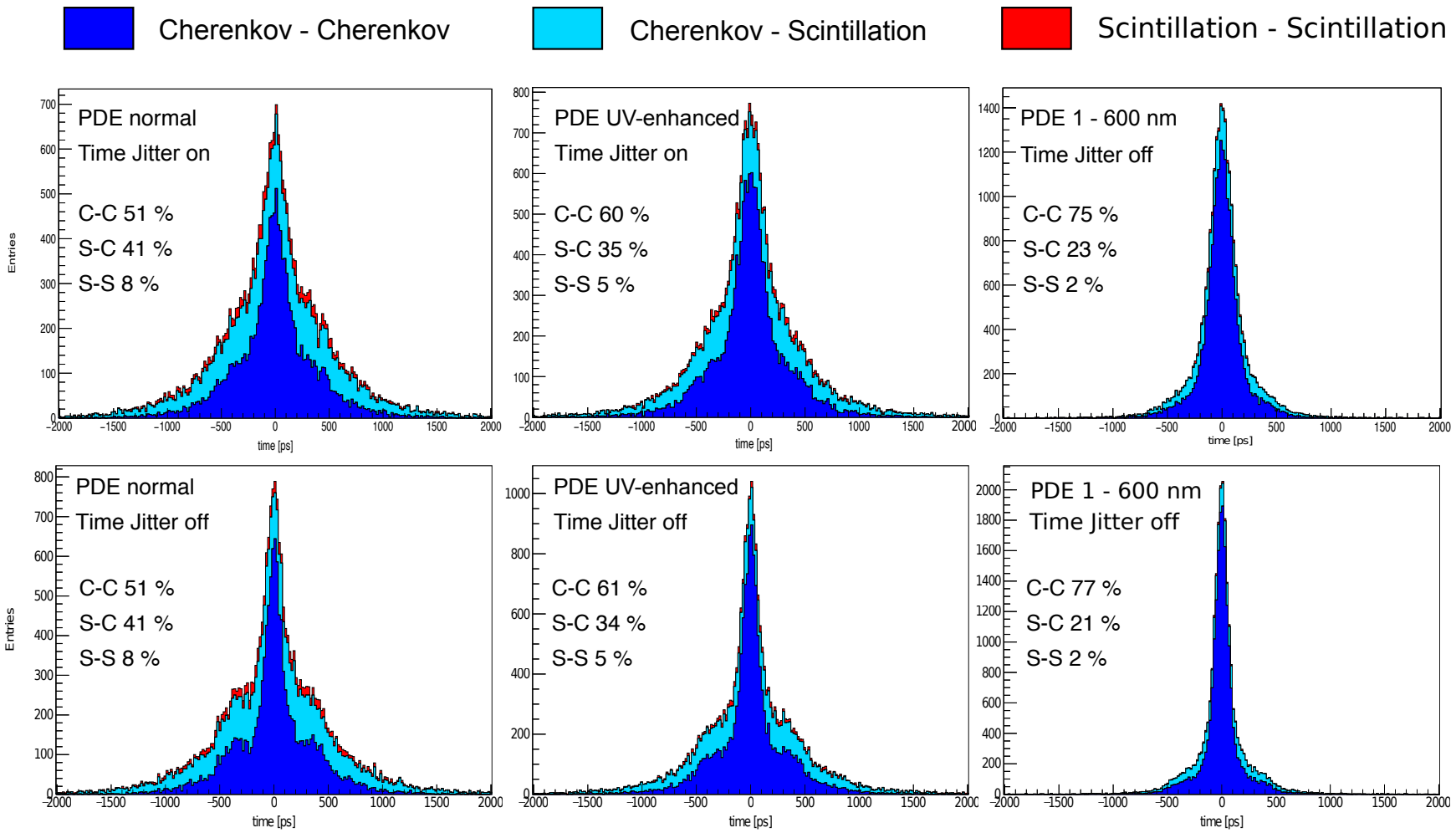

Figure 41: CRT of a polished 3 x 3 x 20 mm^3 BGO crystal with different PDE with and without time jitter for three different cases [41]. All simulations are done with 5 % disabled SPADs.

	Time Jitter On					
	normal PDE		UV-Enhanced		PDE 1- 600 nm	
[%]	Simulated	PAT	Simulated	PAT	Simualted	PAT
C - C	51	50.81	60	59.89	75	75.49
C - S	41	40.94	35	35	23	22.79
S - S	8	8.25	5	5.11	2	1.27
	Time Jitter Off					
C - C	51	51.38	61	61	77	77.1
C - S	41	40.60	34	34.21	21	21.41
S - S	8	8.02	5	4.80	2	1.49

Table 7: Listed is the ratio of the optical photon creation mechanism simulated and calculated with different PDEs. The simulated results are created with n individual correlating annihilation events and the PAT-CRT is calculated with the probability of detecting a concrete photon with the probabilities as shown in Figure 40.

In the analysis excluding the time jitter and real PDE, a broadening of the peak (further called shoulders) in the range $\pm$ 400 ps which could not yet be described is noticed. Since not every generated optical photon is detected due to detector properties (see Figure 31), the CRT is formed by the time difference of the nth generated photon of the first event and by the mth generated photon of the second event. Both detected photons are the first detected photons of the respective event. This results in a mean photon number difference greater zero a Figure 42 shows the photon number difference ($|n - m|$) independent of the CRT. It is obvious, that the mean photon number difference is not null and thereby results in a time difference. Figure 43 shows the CRT on the X-axis and the photon number difference on the Y-axis. There is no assignment to the shoulders due to the different photon number.

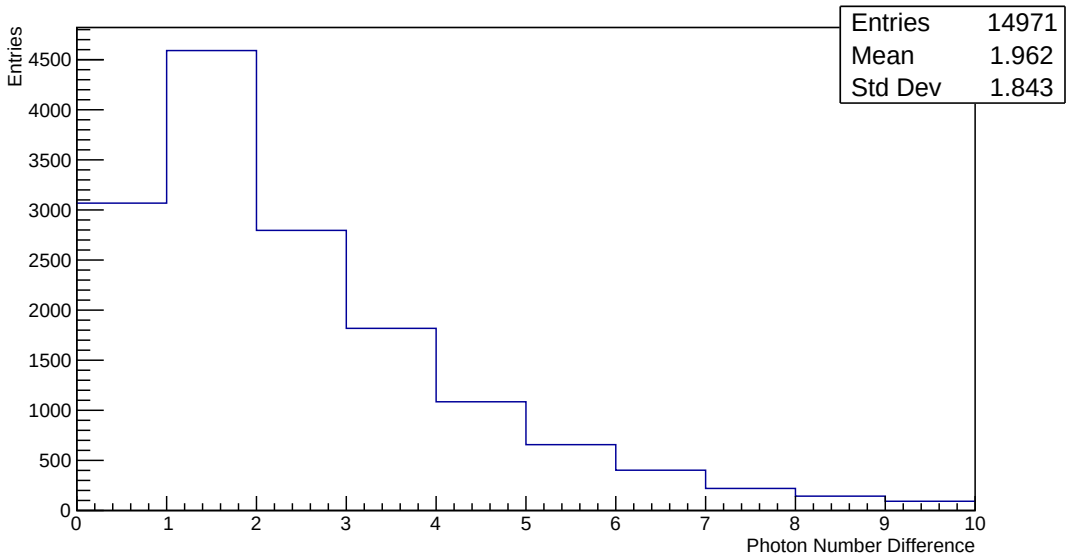

Figure 42: The photon number difference of the first detected photon of the correlating events is shown.

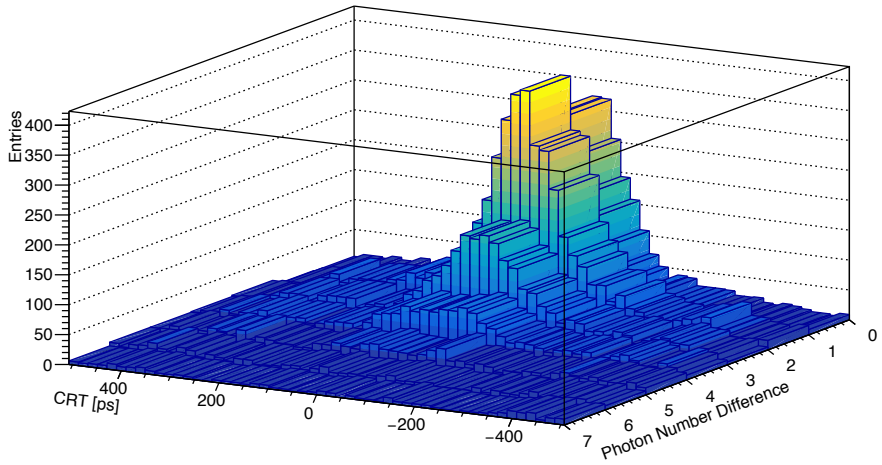

Figure 43: The photon number difference between the first detected optical photons of the correlating events caused the PDE and the CRT of 20 mm BGO polished without time jitter is shown.

It is suggested that the absorption position of the correlating γ-photons is responsible for the shoulders. For the case that both correlating γ-photons were absorbed near the DPC, it is possible that the first detected optical photon of an event is emitted perpendicular to the DPC and the other first detected optical photon of the correlating event is emitted in the opposite way, reflects at the end of the scintillator and propagates back to the detector. This results in a CRT of about 300 ps for a 20 mm long BGO crystal, if the photon is emitted and reflected perpendicular to the DPC. Small changes of this direction results in a larger CRT. Figure 44 shows the CRT on the X-axis and the spatial difference of the γ-photon absorption position of the annihilation photons on the Y-axis. At about $\pm$ 400 ps small elevations for minimum position difference of the correlating γ-photons is apparent, which indicates that the shoulders are created by the mentioned effect.

It is well visible that in the case of positional differences larger than 12 mm, two separate maxima are forms. This time difference maxima are created by the position difference of both events with $\Delta t = \Delta s / c_m$. Δs is the position difference of the absorption position of the correlating γ-photons and c_m is the speed of light in BGO. For 15 mm position difference, a time difference of 111 ps is calculated.

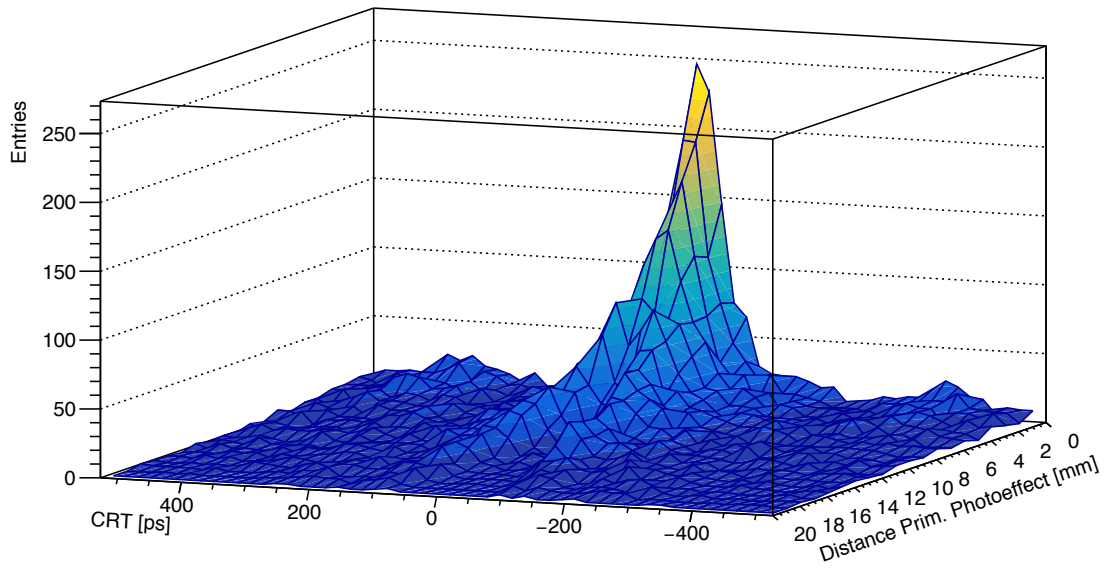

Figure 44: The interaction position difference of the annihilation γ-photons and the corresponding CRT is shown. The two separate maxima above 12 mm are caused by the detection time difference caused by the position difference of the events.

Figure 45 shows the CRT simulated with BGO and BSO, dependent on the surface finishes (ground and polished) and for different crystal lengths. It should be noticed that the results of the CRT between BGO and BSO for different lengths and surface finishes are in the same range. The CRTs show large differences for difference crystal lengths, which are due to different interaction positions of the γ-photon. As a result, a better time resolution can be achieved with smaller crystal lengths. This, however goes along with a lower probability of interaction of the γ-photon with the scintillator as listed in Table 4. The full-width-half-maximum (FWHM) and full-width-tenth-maximum (FWTM) are used for parametrization of the CRT.

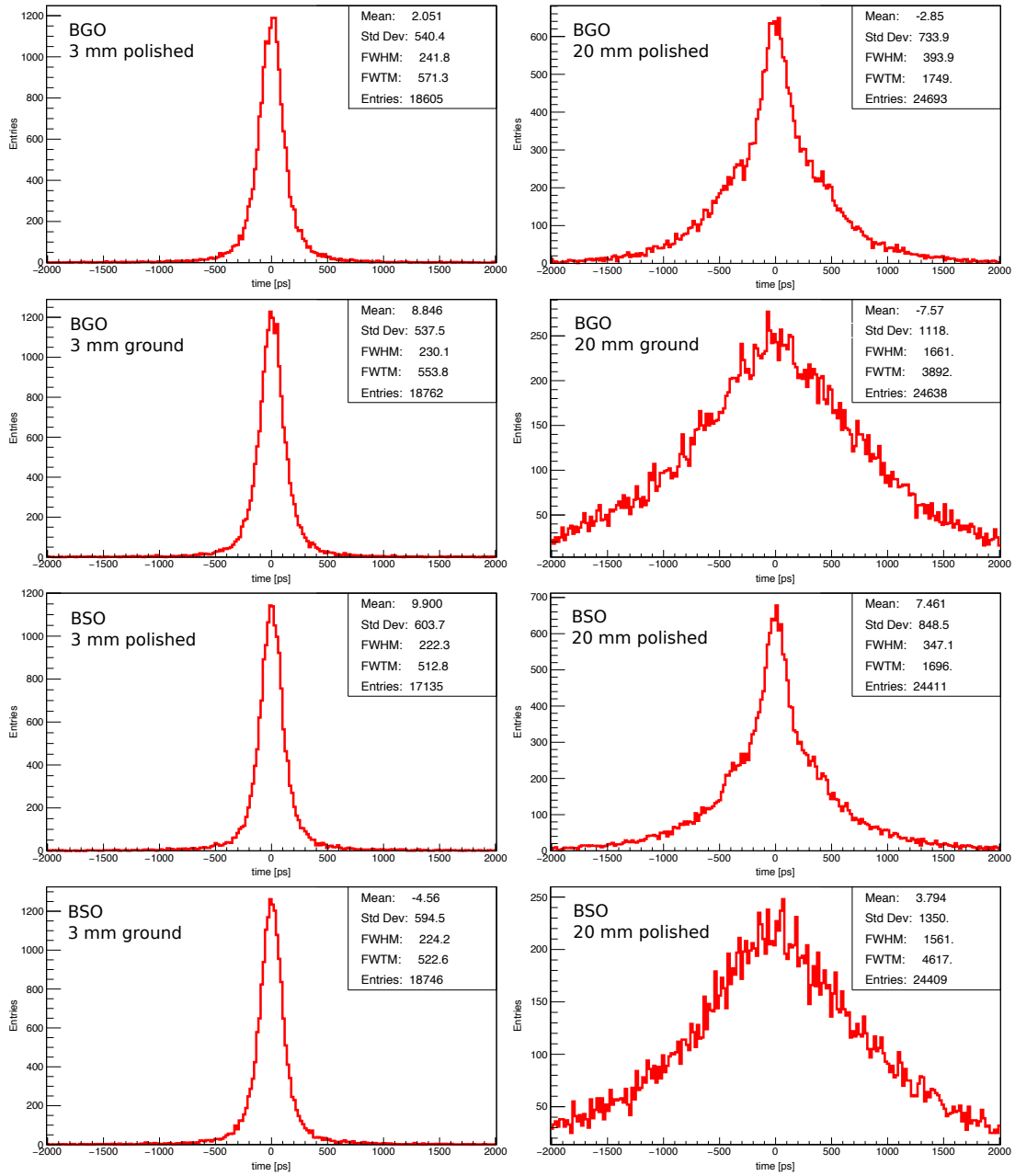

Figure 45: The CRTs of BGO and BSO with different surface finish and crystal length are shown.

Crystal Material	Crystal Length [mm]	Surface Finish	FWHM Simulation [ps]	FWHM Experiment [ps]	FWTM Simulation [ps]	FWTM Experiment [ps]
BGO	3	ground	232	272	556	751
BGO	20	ground	1684	1058	4003	2646
BGO	3	polished	242	252	534	1330
BGO	20	polished	390	411	1807	2631
BSO	3	ground	226	227	519	728
BSO	20	ground	1530	890	4574	3270
BSO	3	polished	220	228	515	1250
BSO	20	polished	349	284	1727	2227

Table 8: Comparison between simulated and measured CRT FWHM and FWTM for BGO and BSO, different surface finishes and crystal length with PDE and inhibit map (5 % disabled SPADs).

Table 8 shows the experimentally determined and simulated FWHM and FWTM of the CRT for BGO and BSO with SPDDIT, inhibit map (5 % disabled SPADs) and time jitter ($\sigma = 50.96$ ps). The relative error of the FWHM varies from 0.35 % - 71.91 % where as the error for 3 mm crystal length is between 0.35 % - 14.73 % and for 20 mm it is between 5.05 % - 71.91 %. The relative error of the FWTM on average is larger and is in the range of 22.45 % - 59.85 %. For a 3 mm long crystal an error of 26.04 % - 59.85 % and for a 20 mm long crystal 22.45 % - 51.31 % was determined. Since the physical properties have already been tested in previous studies, and the theory agrees well, the partly large errors are presumed to be due to the dependence of the CRT on the crystal surface finish. In the appendix, some simulation data with different simulation parameters are listed. It is shown that the dependence of the simulation results is essentially dependent on the type of surface simulation. It was mainly simulated with the Look-Up-Table in GEANT4. In order to achieve the best possible simulation with the unified model, all parameters must be optimized as described in section 2.4.2.2 which can be done with further simulations but is an extensive work which goes beyond the scope of this work.

Figure 46 shows the simulated and experimentally determined CRT of a 3 x 3 x 3 mm^3 large BGO scintillator crystal. A polished surface with 5 % inhibit map, SPAD time jitter and PDE was simulated. Experimental data on polished and unpolished surface texture is presented. The simulation data was again divided into three categories depending on the photon creating process. It becomes apparent that the main creation process responsible for the CRT is the Cherenkov effect. The detected Cherenkov Photons photons are mainly located approximately between -1 and 1 ns. Events in which one detected photon is generated by scintillation and one by the Cherenkov effect contribute to the complete CRT spectrum and have a ratio of about 21 %. The ratio of coincidences formed by scintillation photons only is about 2 % and therefore contributes little to the CRT. The FWHM of the simulation and measured data are comparable but differ for FWTM, as listed in Table 8. It is assumed that the FWTM of the CRT depends essentially on the surface characteristics of the scintillator which is hard to be simulated.

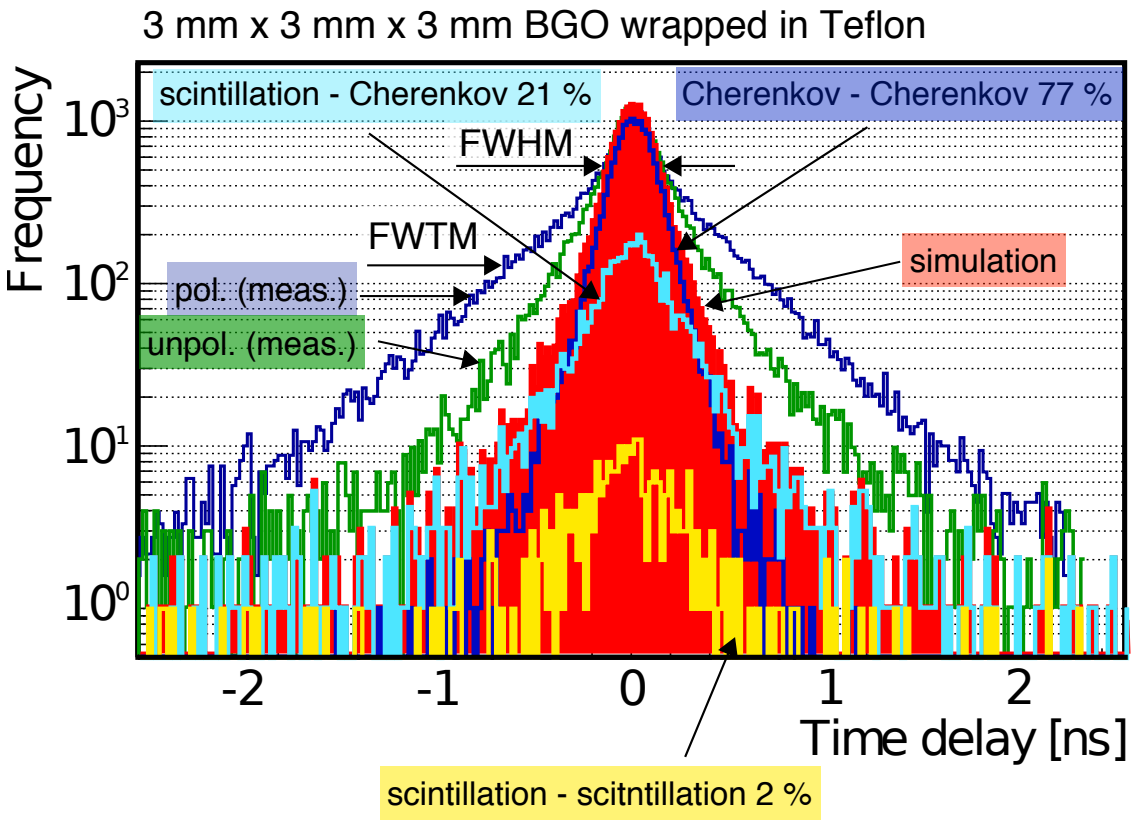

Figure 46: A comparison of the CRT between the measured and simulated data of a 3 mm long BGO scintillation crystal is shown [41].

5 Conclusion

The scintillation crystals BGO and BSO were implemented into an existing simulation package and their physical properties such as free path length of optical photons, absorption length of 511 keV γ-photons, created scintillation photons and created Cherenkov photons have been tested and shows qualitative agreement with the theory of radiation by moving chargers and theory of scintillation [40, 42]. Simulations and analyses were performed with scintillators of the dimension of 3 x 3 x 3 mm^3 and 3 x 3 x 20 mm^3.

Furthermore, detector properties of the dSiPM developed by Philips such as photon detection efficiency, single photon detection during integration time, inhibit map and time jitter were taken into account. Three different PDEs, the measured PDE [35] a UV-enhanced PDE and a perfect PDE of 1 between 273 - 600 nm were implemented and compared. It was shown, that with an improved PDE in the UV, the CRT improves and the probability that coincidences are formed only by Cherenkov photons increases. It could be shown the CRT is mainly formed by Cherenkov photons. This is despite the small number of generated Cherenkov photons compared to generated scintillations photons. This is due to the almost instantaneous emission of Cherenkov photons and the relatively high Cherenkov photon number compared to other scintillator materials due to the high refractive index and high atomic number of BGO and BSO. The FWHM of the CRT compared to values published in [7] agrees with the measured values with errors in the single-digit percentage range for polished scintillators but are larger for unpolished scintillators and diverge more widely for both surface conditions for the FWTM. It is assumed that these discrepancies are due to the incorrect simulation of the scintillator surface. To confirm or refute this, further simulations must be carried out.

The detected photon number was also compared with experimentally determined data. Here, the errors except for the configuration BGO polished are located within 20 %. It is again assumed that this depends on the surface simulation in GEANT4 and must be investigated in further simulations.

The differences in the number of photons detected by BGO due to the surface simulations of the scintillator were examined for the Glisur and Look-Up-Table models provided by GEANT4. No significant differences could be found since all results are within a small range. Further simulation based on the unified model must be made in order to optimize the simulation.

The present GEANT4 simulation is a base for simulating the experiments planned in the PALADIN project [4]. In order to make trustworthy predictions, further simulations must be carried out and the system has to be optimized. The physics models provided by GEANT4 should be compared as well as the simulation of the surface of the scintillator, which provides a significant contribution to the CRT as well as the number of detected photons. In order to reduce the computation time, which is particularly advantageous for future more complex simulations such as a detector ring, the multi-threading supported by GEANT4 can be implemented. After optimizing the application, continuing simulations can be made to make predictions and thereby achieve an improved time resolution of detector systems for positron annihilation detection.

List of Figures

List of Tables

References

[1] G. F. Knoll, *Radiation Detection and Measurement; 3rd ed.* New York, NY: Wiley, 2000.

[2] T. Frach, G. Prescher, C. Degenhardt, R. de Gruyter, A. Schmitz, and R. Ballizany, "The digital silicon photomultiplier - Principle of operation and intrinsic detector performance," in *2009 IEEE Nuclear Science Symposium Conference Record (NSS/MIC)*, pp. 1959–1965, Oct 2009.

[3] W. W. Moses and S. E. Derenzo, "Prospects for time-of-flight PET using LSO scintillator," *IEEE Transactions on Nuclear Science*, vol. 46, pp. 474–478, Jun 1999.

[4] "PALADIN project." https://fasttiming.weebly.com/.

[5] F. Dachs, "Monte-Carlo simulation of a new ultra-fast gamma detector design in Geant4," 2016. Diplomarbeit Technische Universität Wien 2017.

[6] S. Agostinelli, J. Allison, K. Amako, J. Apostolakis, H. Araujo, P. Arce, M. Asai, D. Axen, S. Banerjee, G. Barrand, F. Behner, L. Bellagamba, J. Boudreau, L. Broglia, A. Brunengo, H. Burkhardt, S. Chauvie, J. Chuma, R. Chytracek, G. Cooperman, G. Cosmo, P. Degtyarenko, A. Dell'Acqua, G. Depaola, D. Dietrich, R. Enami, A. Feliciello, C. Ferguson, H. Fesefeldt, G. Folger, F. Foppiano, A. Forti, S. Garelli, S. Giani, R. Giannitrapani, D. Gibin, J. G. Cadenas, I. González, G. G. Abril, G. Greeniaus, W. Greiner, V. Grichine, A. Grossheim, S. Guatelli, P. Gumplinger, R. Hamatsu, K. Hashimoto, H. Hasui, A. Heikkinen, A. Howard, V. Ivanchenko, A. Johnson, F. Jones, J. Kallenbach, N. Kanaya, M. Kawabata, Y. Kawabata, M. Kawaguti, S. Kelner, P. Kent, A. Kimura, T. Kodama, R. Kokoulin, M. Kossov, H. Kurashige, E. Lamanna, T. Lampén, V. Lara, V. Lefebure, F. Lei, M. Liendl, W. Lockman, F. Longo, S. Magni, M. Maire, E. Medernach, K. Minamimoto, P. M. de Freitas, Y. Morita, K. Murakami, M. Nagamatu, R. Nartallo, P. Nieminen, T. Nishimura, K. Ohtsubo, M. Okamura, S. O'Neale, Y. Oohata, K. Paech, J. Perl, A. Pfeiffer, M. Pia, F. Ranjard, A. Rybin, S. Sadilov, E. D. Salvo, G. Santin, T. Sasaki, N. Savvas, Y. Sawada, S. Scherer, S. Sei, V. Sirotenko, D. Smith, N. Starkov, H. Stoecker, J. Sulkimo, M. Takahata, S. Tanaka, E. Tcherniaev, E. S. Tehrani, M. Tropeano, P. Truscott, H. Uno, L. Urban, P. Urban, M. Verderi, A. Walkden, W. Wander, H. Weber, J. Wellisch, T. Wenaus, D. Williams, D. Wright, T. Yamada, H. Yoshida, and D. Zschiesche, "Geant4—a simulation toolkit," *Nuclear Instruments and Methods in Physics Research Section A: Accelerators, Spectrometers, Detectors and Associated Equipment*, vol. 506, no. 3, pp. 250 – 303, 2003.

[7] S. E. Brunner and D. R. Schaart, "BGO as a hybrid scintillator / Cherenkov radiator for cost-effective time-of-flight PET," *Physics in Medicine Biology*, vol. 62, no. 11, p. 4421, 2017.

[8] R. Brun and F. Rademakers, "Root — an object oriented data analysis framework," *Nuclear Instruments and Methods in Physics Research Section A: Accelerators, Spectrometers, Detectors and Associated Equipment*, vol. 389, no. 1, pp. 81 – 86, 1997. New Computing Techniques in Physics Research V.

[9] G. Cowan, *Statistical data analysis.* Oxford University Press, USA, 1998.

[10] Geant4-Collaboration, "Geant4 User's Guide for Application Developers," 2015.

[11] M. J. Berger, J. H. Hubbell, S. M. Seltzer, J. Chang, J. S. Coursey, R. Sukumar, D. S. Zucker, and K. Olsen, "Xcom: Photon cross section datadata," *http://physics.nist.gov/xcom*, vol. no. Verison 1.5, 2010.

[12] Nuclear Power, "Interaction of gamma radiation with matter." `http://www.nuclear-power.net/nuclear-power/reactor-physics/interaction-radiation-matter/interaction-gamma-radiation-matter/`, November 2017.

[13] C. M. Davisson, "Interaction of γ-RADIATION with Matter," in *Alpha-, Beta- and Gamma-ray Spectroscopy* (K. Siegbahn, ed.), p. 37, 1965.

[14] P. Riis, "Texample.net." `http://www.texample.net/tikz/examples/gamma-interaction/`, January 2018.

[15] W. Demtröder, *Experimentalphysik 2 Elektrizität und Optik*, vol. 495. Springer-Verlag Berlin Heidelberg, 5 ed., 2009.

[16] M. Janecek and W. W. Moses, "Simulating Scintillator Light Collection Using Measured Optical Reflectance," *IEEE Transactions on Nuclear Science*, vol. 57, pp. 964–970, June 2010.

[17] A. Levin and C. Moisan, "A more physical approach to model the surface treatment of scintillation counters and its implementation into DETECT," in *1996 IEEE Nuclear Science Symposium. Conference Record*, vol. 2, pp. 702–706 vol.2, Nov 1996.

[18] M. Janecek and W. W. Moses, "Measuring Light Reflectance of BGO Crystal Surfaces," *IEEE Transactions on Nuclear Science*, vol. 55, pp. 2443–2449, Oct 2008.

[19] E. Dietz-laursonn, "Peculiarities in the simulation of optical physics with geant4," 12 2016.

[20] D. Renker, "Geiger-mode avalanche photodiodes, history, properties and problems," *Nuclear Instruments and Methods in Physics Research Section A: Accelerators, Spectrometers, Detectors and Associated Equipment*, vol. 567, no. 1, pp. 48 – 56, 2006. Proceedings of the 4th International Conference on New Developments in Photodetection.

[21] E. Roncali and S. R. Cherry, "Application of Silicon Photomultipliers to Positron Emission Tomography," *Annals of Biomedical Engineering*, vol. 39, pp. 1358–1377, 04 2011.

[22] H. T. van Dam, S. Seifert, R. Vinke, P. Dendooven, H. Lohner, F. J. Beekman, and D. R. Schaart, "A Comprehensive Model of the Response of Silicon Photomultipliers," *IEEE Transactions on Nuclear Science*, vol. 57, pp. 2254–2266, Aug 2010.

[23] S. Brunner, L. Gruber, A. Hirtl, K. Suzuki, J. Marton, and D. Schaart, "A comprehensive characterization of the time resolution of the Philips Digital Photon Counter," *Journal of Instrumentation*, vol. 11, no. 11, p. P11004, 2016.

[24] R. Schulze, "Tile-TEK Manual v1.00." Philips Digital Photon Counting, 2015.

[25] M. Nemallapudi, S. Gundacker, P. Lecoq, and E. Auffray, "Single photon time resolution of state of the art SiPMs," *Journal of Instrumentation*, vol. 11, no. 10, p. P10016, 2016.

[26] S. E. Brunner, *Fast single photon detection for scintillation and Cherenkov applications using Silicon Photomultipliers.* AC11996520, Vienna University of Technology, PhD Thesis, 2014.

[27] Y. Haemisch, T. Frach, C. Degenhardt, and A. Thon, "Fully digital arrays of silicon photomultipliers (dsipm) – a scalable alternative to vacuum photomultiplier tubes (pmt)," *Physics Procedia*, vol. 37, pp. 1546 – 1560, 2012. Proceedings of the 2nd International Conference on Technology and Instrumentation in Particle Physics (TIPP 2011).

[28] S. Seifert, H. T. van Dam, and D. R. Schaart, "The lower bound on the timing resolution of scintillation detectors," *Physics in Medicine & Biology*, vol. 57, no. 7, p. 1797, 2012.

[29] M. H. DeGroot and M. J. Schervish, *Probability and Statistics.* Addison Wesley, 3rd ed., 2002.

[30] I. Holl, E. Lorenz, and G. Mageras, "A measurement of the light yield of common inorganic scintillators," *IEEE Transactions on Nuclear Science*, vol. 35, pp. 105–109, Feb 1988.

[31] M. Moszyński, C. Gresset, J. Vacher, and R. Odru, "Timing properties of BGO scintillator," *Nuclear Instruments and Methods in Physics Research*, vol. 188, no. 2, pp. 403 – 409, 1981.

[32] R. Mao, L. Zhang, and R.-Y. Zhu, "Optical and scintillation properties of inorganic scintillators in high energy physics," *IEEE Trans. Nucl. Sci.*, vol. 55, pp. 2425–2431, 2008.

[33] P. A. Williams, A. H. Rose, K. S. Lee, D. C. Conrad, G. W. Day, and P. D. Hale, "Optical, thermo-optic, electro-optic, and photoelastic properties of bismuth germanate (Bi4Ge3O12)," *Appl. Opt.*, vol. 35, pp. 3562–3569, Jul 1996.

[34] D. P. Bortfeld and H. Meier, "Refractive indices and electrooptic coefficients of the eulitities $Bi_4Ge_3O_{12}$ and $Bi_4Si_3O_{12}$," *Journal of Applied Physics*, vol. 43, no. 12, pp. 5110–5111, 1972.

[35] "DPC3200-22-44 Datasheet." Philips Digital Photon Counting, 2015.

[36] M.-A. Verdier, P. C. F. di Stefano, P. Nadeau, C. Behan, M. Clavel, and C. Dujardin, "Scintillation properties of $Bi_4Ge_3O_{12}$ down to 3 K under γ rays," *Phys. Rev. B*, vol. 84, p. 214306, Dec. 2011.

[37] B. Yang, J. Xu, Y. Zhang, H. Zeng, T. Tian, Y. Chu, Y. Pan, and Q. Cui, "Improvement and luminescent mechanism of $Bi_4Si_3O_{12}$ scintillation crystals by Dy_{3+} doping," *Nuclear Instruments and Methods in Physics Research Section A: Accelerators, Spectrometers, Detectors and Associated Equipment*, vol. 807, pp. 1 – 4, 2016.

[38] P. Lecoq, A. Gektin, and M. Korzhik, *Inorganic Scintillators for Detector Systems: Physical Principles and Crystal Engineering.* Particle Acceleration and Detection, Springer International Publishing, 2016.

[39] W. Wolszczak, M. Moszyński, T. Szczęśniak, M. Grodzicka, and K. Kacperski, "Temperature properties of scintillators for PET detectors: A comparative study," in *2014 IEEE Nuclear Science Symposium and Medical Imaging Conference (NSS/MIC)*, pp. 1–4, Nov 2014.

[40] J. D. Jackson, *Classical electrodynamics.* New York, NY: Wiley, 3rd ed. ed., 1999.

[41] S. E. Brunner, F. Dachs, M. Gruber, A. Hirtl, K. Kamman, and D. R. Schaart, "SCINT Conference," *Charmonix*, Sep., 20. 2017.

[42] J. Birks, D. Fry, L. Costrell, and K. Kandiah, *The Theory and Practice of Scintillation Counting: International Series of Monographs in Electronics and Instrumentation.* International series of monographs on electronics and instrumentation, Elsevier Science, 2013.

A GEANT4 Unified Model Optical Surfaces

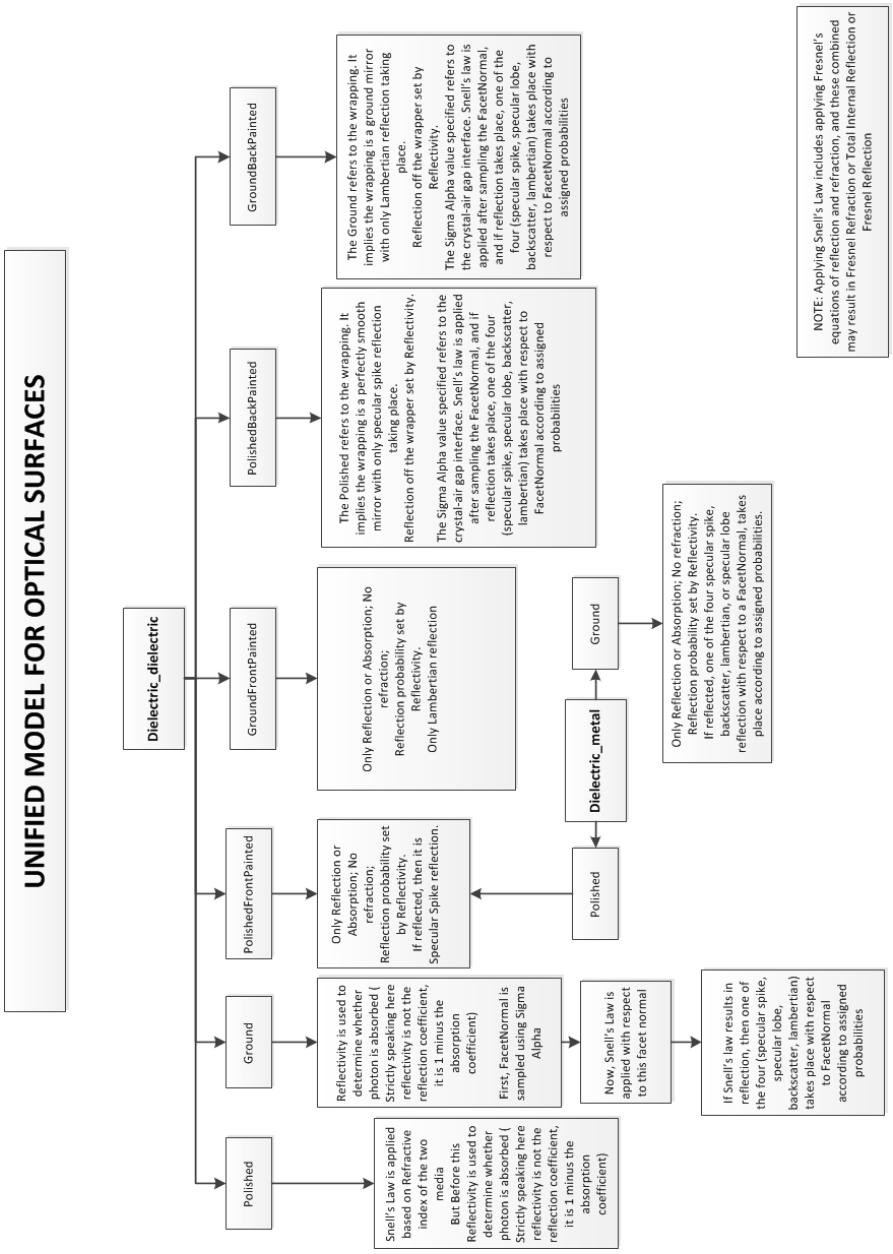

Figure 47: Shown are the selectable surface types of the unified model and their properties [10].

B Additional Tables

Crystal Material	Crystal Length [mm]	Surface Type	Sigma Alpha	Photon Detection Efficiency	reflection correction	Light yield [photons]	rise time [ns]	fast decay time [ns]	slow decay time [ns]	yield ratio	resolution scale	Single Phot. Detection	air gap	inh. cells [%]	Integration Time [ns]	Time Jitter Sigma [ps]	FWHM [ps]	FWTM [ps]
BGO	3	ground	0,09	normal	yes	8200	0,05	60	300	0,1	3,15	on	yes	5	650	50,96	212,5	446,5
BGO	20	ground	0,09	normal	yes	8200	0,05	60	300	0,1	3,15	on	yes	5	650	50,96	1421	3143
BGO	3	polished	-	normal	yes	8200	0,05	60	300	0,1	3,15	on	no	5	650	50,96	210,6	446,5
BGO	20	polished	-	normal	yes	8200	0,05	60	300	0,1	3,15	on	no	5	650	50,96	323,7	1300
BSO	3	ground	0,09	normal	yes	1640	0,05	-	100	-	3,022	on	yes	5	650	50,96	196,9	438,7
BSO	20	ground	0,09	normal	yes	1640	0,05	-	100	-	3,022	on	yes	5	650	50,96	1222	3603
BSO	3	polished	-	normal	yes	1640	0,05	-	100	-	3,022	on	no	5	650	50,96	202,8	430,9
BSO	20	polished	-	normal	yes	1640	0,05	-	100	-	3,022	on	no	5	650	50,96	298,3	1314
BGO	3	ground	0,09	uv-enhanced	yes	8200	0,05	60	300	0,1	3,15	on	yes	5	650	50,96	177,4	374,4
BGO	20	ground	0,09	uv-enhanced	yes	8200	0,05	60	300	0,1	3,15	on	yes	5	650	50,96	1199	2811
BGO	3	polished	-	uv-enhanced	yes	8200	0,05	60	300	0,1	3,15	on	no	5	650	50,96	179,4	368,5
BGO	20	polished	-	uv-enhanced	yes	8200	0,05	60	300	0,1	3,15	on	no	5	650	50,96	271	1074
BSO	3	ground	0,09	uv-enhanced	yes	1640	0,05	-	100	-	3,022	on	yes	5	650	50,96	173,5	352,9
BSO	20	ground	0,09	uv-enhanced	yes	1640	0,05	-	100	-	3,022	on	yes	5	650	50,96	1095	3416
BSO	3	polished	-	uv-enhanced	yes	1640	0,05	-	100	-	3,022	on	no	5	650	50,96	175,5	349
BSO	20	polished	-	uv-enhanced	yes	1640	0,05	-	100	-	3,022	on	no	5	650	50,96	257,4	943,8
BGO	3	ground	0,09	PDE = 1 between 273-600 nm	yes	8200	0,05	60	300	0,1	3,15	on	yes	5	650	50,96	159,9	317,8
BGO	20	ground	0,09	PDE = 1 between 273-600 nm	yes	8200	0,05	60	300	0,1	3,15	on	yes	5	650	50,96	848,2	2158
BGO	3	polished	-	PDE = 1 between 273-600 nm	yes	8200	0,05	60	300	0,1	3,15	on	no	5	650	50,96	165,7	319,8
BGO	20	polished	-	PDE = 1 between 273-600 nm	yes	8200	0,05	60	300	0,1	3,15	on	no	5	650	50,96	253,5	785,8
BSO	3	ground	0,09	PDE = 1 between 273-600 nm	yes	1640	0,05	-	100	-	3,022	on	yes	5	650	50,96	154	304,2
BSO	20	ground	0,09	PDE = 1 between 273-600 nm	yes	1640	0,05	-	100	-	3,022	on	yes	5	650	50,96	912,6	2369
BSO	3	polished	-	PDE = 1 between 273-600 nm	yes	1640	0,05	-	100	-	3,022	on	no	5	650	50,96	157,9	308,1
BSO	20	polished	-	PDE = 1 between 273-600 nm	yes	1640	0,05	-	100	-	3,022	on	no	5	650	50,96	224,2	618,1

Table 9: Simulated CRTs with different input parameter I.

Crystal Material	Crystal Length [mm]	Surface Type	Sigma Alpha	Photon Detection Efficiency	reflection correction	Light yield [photons]	rise time [ns]	fast decay time [ns]	slow decay time [ns]	yield ratio	resolution scale	Single Phot. Detection	air gap	inh. cells [%]	Integration Time [ns]	Time Jitter Sigma [ps]	FWHM [ps]	FWTM [ps]
BGO	3	ground	0,09	normal	yes	8200	0,05	60	300	0,1	3,15	on	yes	5	650	0	83,85	282,7
BGO	20	ground	0,09	normal	yes	8200	0,05	60	300	0,1	3,15	on	yes	5	650	0	1220	3041
BGO	3	polished	-	normal	yes	8200	0,05	60	300	0,1	3,15	on	no	5	650	0	58,5	273
BGO	20	polished	-	normal	yes	8200	0,05	60	300	0,1	3,15	on	no	5	650	0	191,1	1084
BSO	3	ground	0,09	normal	yes	1640	0,05	-	100	-	3,022	on	yes	5	650	0	66,3	249,6
BSO	20	ground	0,09	normal	yes	1640	0,05	-	100	-	3,022	on	yes	5	650	0	1273	3786
BSO	3	polished	-	normal	yes	1640	0,05	-	100	-	3,022	on	no	5	650	0	58,50	247,6
BSO	20	polished	-	normal	yes	1640	0,05	-	100	-	3,022	on	no	5	650	0	161,8	1029
BGO	3	polished	-	normal	yes	8200	0,05	60	300	0,1	3,15	on	yes	5	650	0	95,55	222,3
BGO	20	polished	-	normal	yes	8200	0,05	60	300	0,1	3,15	on	yes	5	650	0	208,6	1144
BGO	3	polished	-	normal	yes	8200	0,05	60	300	0,1	3,15	on	yes	5	650	50,96	191,1	366,6
BGO	20	polished	-	normal	yes	8200	0,05	60	300	0,1	3,15	on	yes	5	650	50,96	349	1238
BSO	3	polished	-	normal	yes	1640	0,05	-	100	-	3,022	on	yes	5	650	50,96	181,3	362,7
BSO	20	polished	-	normal	yes	1640	0,05	-	100	-	3,022	on	yes	5	650	50,96	312	1255
BGO	3	ground	0,09	normal	no	8200	0,05	60	300	0,1	3,15	on	yes	5	650	50,96	232	555,7
BGO	20	ground	0,09	normal	no	8200	0,05	60	300	0,1	3,15	on	yes	5	650	50,96	1684	4003
BGO	3	polished	-	normal	no	8200	0,05	60	300	0,1	3,15	on	no	5	650	50,96	241,8	534,3
BGO	20	polished	-	normal	no	8200	0,05	60	300	0,1	3,15	on	no	5	650	50,96	390	1807
BSO	3	ground	0,09	normal	no	1640	0,05	-	100	-	3,022	on	yes	5	650	50,96	226,2	518,7
BSO	20	ground	0,09	normal	no	1640	0,05	-	100	-	3,022	on	yes	5	650	50,96	1530	4574
BSO	3	polished	-	normal	no	1640	0,05	-	100	-	3,022	on	no	5	650	50,96	220,3	514,8
BSO	20	polished	-	normal	no	1640	0,05	-	100	-	3,022	on	no	5	650	50,96	349	1727
BGO	3	ground	0,09	normal	yes	8200	0,05	60	300	0,1	3,15	on	yes	5	650	50,96	189,1	432,9
BGO	20	ground	0,09	normal	yes	8200	0,05	60	300	0,1	3,15	on	yes	5	650	50,96	1113	3205
BGO	3	ground	0,09	normal	yes	8200	0,05	60	300	0,1	3,15	on	yes	5	650	50,96	198,9	446,5
BGO	20	ground	0,09	normal	yes	8200	0,05	60	300	0,1	3,15	on	yes	5	650	50,96	1443	3465

Table 10: Simulated CRTs with different input parameter II.